FAK modulates glioblastoma stem cell energetics via actomyosin contractility: regulation of glycolysis and mitochondrial function

Roza H. Ali Masalmeh[1], John C. Dawson[1], Virginia Alvarez Garcia[1,2], Morwenna T. Muir[1], Roderick N. Carter[3], Giles Hardingham[3,4,5], Cameron Davies[1], Rosina Graham[1], Alex von Kriegsheim[1], Jair Marques Junior[1], Chinmayi Pednekar[1], Steven M. Pollard[6], Neil O. Carragher[1], Valerie G. Brunton[1], Margaret C Frame[1].

[1]Cancer Research UK Scotland Centre (Edinburgh), Institute of Genetics and Cancer, University of Edinburgh, Crewe Road South, Edinburgh EH4 2XU, UK.

[2]Department of Physiology and Pharmacology, School of Medicine, University of Cantabria and Instituto de Investigacion Valdecilla (IDIVAL), 39011 Santander, Spain.

[3]UK Dementia Research Institute, Chancellor's Building, University of Edinburgh, 49 Little France Crescent, Edinburgh, UK

[4]Simons Initiative for the Developing Brain, University of Edinburgh, Edinburgh, United Kingdom.

[5]Centre for Discovery Brain Sciences, Hugh Robson Building, University of Edinburgh, Edinburgh, United Kingdom.

[6]Centre for Regenerative Medicine, Institute for Regeneration and Repair, University of Edinburgh, 5 Little France Drive, Edinburgh EH16 4UU, UK.

Correspondence:

roza.masalmeh@ed.ac.uk (R.H.A.M.)

m.frame@ed.ac.uk (M.C.F.)

Abstract

Glycolysis and the TCA cycle are commonly reprogrammed to fulfil the bioenergetic and biosynthetic demands of cancer cells. Although the extracellular matrix is known to influence glycolysis and the TCA cycle, it is not well understood how specific adhesion proteins and their downstream effectors contribute to metabolic changes and to the mitigation of metabolic stress. Here, we report that the canonical focal adhesion protein FAK is required for optimal cellular energetics through both glycolysis and the TCA cycle in a transformed neural stem cell model of glioblastoma. Mechanistically, FAK promotes the TCA cycle by keeping myosin

II activity low in cells with a mesenchymal-like morphology. Genetic deletion of FAK induces an epithelial-like morphology with elevated myosin II activity as evidenced by phospho-myosin light chain accumulation at cell-cell contacts. In this context these cells have impaired glycolysis and TCA cycle flux that is accompanied by shortening of mitochondria fragments. Phenotypically, the reduction in cell energetics after FAK depletion is accompanied by reduced cancer cell motility and invasiveness in vitro and suppression of tumour growth and increased survival in orthotopic murine models. We demonstrate a novel role for FAK as an adhesion protein which can modulate cellular energetics and mitochondria morphology in glioblastoma stem cells with profound consequences for cancer-associated cell phenotypes and tumour growth in vivo.

Introduction

Glioblastoma (GBM) is the most common and lethal form of malignant primary brain tumour [1]. The standard treatment for this cancer involves surgical resection, radiation therapy and chemotherapy. However, none of these are curative. One of the reasons why GBM is resistant to therapy is because of the presence of a subset of cells within the tumour with high tumorigenic capacity, termed GBM stem cells[2,3]. These cells can drive recurrence and heterogeneity by rewiring their signalling and metabolism to adapt to restricted nutrition and overcome therapies[4]. The ability of cancer cells to reprogram energy metabolism has emerged as a hallmark of cancer and their ability to shift between different metabolic states has been recently recognized as a therapeutic target [5,6]. A recent study, investigating biological traits of human GBM tumours, revealed at least four tumour cell states: proliferative/progenitor, neuronal, mitochondrial and glycolytic/plurimetabolic [7]. GBM stem cells classified in the mitochondrial state critically depends on oxidative phosphorylation (OXPHOS) to produce energy whereas the glycolytic/plurimetabolic subtype utilises multiple energy-producing pathways, e.g., glycolysis, amino acid and lipid metabolism, granting cancer cells metabolic adaptability and protection from oxidative stress and cell death. Amongst the four subtypes, the mitochondrial subtype had significantly better clinical outcome and is more susceptible to

61 OXPHOS inhibitors[7]. This highlights the importance of understanding metabolic pathways in
62 GBM and the potential for finding metabolic vulnerabilities that we can exploit therapeutically.

63 One of the ways by which metabolism is altered in cancers is through responding to cues from
64 the tumour microenvironment. For example, increasing extracellular matrix (ECM) stiffness
65 can modulate glycolysis, increase the activity of metabolic enzymes, affect mitochondria
66 morphology and function [8–10]. These alterations help cancer cells resist oxidative stress and
67 promote the development of invasive and metastatic phenotypes. The actin cytoskeleton can
68 function as a scaffold for some glycolytic enzymes which can modulate glycolysis through
69 spatial and functional regulation of these enzymes[11]. An unanswered question is whether, and
70 how, this is connected to the role of dynamic actin remodelling in processes such as cell
71 migration or hallmark changes in cell state, such as epithelial-to-mesenchymal transition
72 (EMT). The links between cell-ECM mechanical cues, the actin cytoskeleton and metabolism
73 are beginning to be identified yet we do not know which integrin may contribute.

74 Focal Adhesion Kinase (FAK) is a key signal transduction regulator found at integrin adhesions
75 [12,13]. Indeed, FAK is at the centre of one of the four focal adhesion nexuses that connect
76 integrin complexes to actin and multiple intracellular signalling axes[13]. FAK is also known to
77 buffer adhesion and therapeutic stress in tumour cells and promote their survival [14]. In the
78 context of GBM, integrin adhesion related genes (e.g., *ITGB1* and *PTK2*) are essential genetic
79 dependencies for the injury-response transcriptional state as defined by Richards et al[15,16].

80 We therefore set out to address the role of FAK in a transformed neural stem cell model of
81 GBM that we have recently described [17,18] and specifically address whether FAK could link the
82 regulation of adhesion signalling to metabolic pathways, and if so, uncover the mechanism.
83 We found that FAK expression was increased upon oncogenic transformation and that
84 CRISPR/Cas9-mediated genetic deletion of FAK reduced tumour growth in vivo. FAK deletion
85 in these cells induced a profound change in both cellular morphology, and the actin
86 cytoskeleton along with concomitant changes in gene expression consistent with transition
87 from a mesenchymal to epithelial-like phenotype. As a result of these changes, cells were

88 significantly less motile both in 2-dimensional culture and in 3-dimensional invasion assays.
89 Furthermore, loss of FAK significantly suppressed rates of both glycolysis and OXPHOS. This
90 was associated with enhanced actomyosin contractility especially evident at cell-cell contacts
91 and alterations in mitochondria morphology. FAK-dependent mesenchymal morphology,
92 spatial phospho-myosin light chain (p-MLC), the TCA cycle activity and mitochondria
93 morphology were restored by treatment with multiple Rho-kinase (ROCK) inhibitors.
94 Therefore, FAK co-regulates actin, actomyosin contractility, migration and invasion via ROCK
95 in a transformed neural stem cell GBM model and we show here that this is linked to FAK-
96 regulated mitochondrial morphology and cellular energetics. This describes a new cellular
97 dependency regulated by FAK in GBM cells.

98 **Results**

99 **FAK controls GBM-associated cellular phenotypes**

100 The underlying mechanisms by which FAK may contribute to GBM are poorly understood. We
101 examined FAK's role in GBM using a disease-relevant transformed mouse neural stem cell
102 model that we have described previously [17,18]. The neural stem cell model is important
103 because neural stem cells are believed to be one of the potential cells of origin of GBM and
104 that they give rise to GBM stem cells which are thought to drive recurrence and therapeutic
105 resistance [19]. We used neural stem cells which have been modified to harbour co-deletion of
106 the genes encoding neurofibromatosis type 1 (*Nf1*) and phosphatase and tensin homolog
107 (*Pten*) and over-expression of the epidermal growth factor receptor variant III (EGFRvIII)
108 (termed NPE cells). We found that the mRNA levels of *Ptk2*, the mouse gene encoding FAK,
109 is significantly increased in transformed NPE cells when compared to untransformed parental
110 neural stem cells ($p<0.0001$) (Figure 1A), and increased *Ptk2* expression is paralleled by
111 elevated FAK protein levels in NPE cells (Figure 1B). CRISPR-Cas9-mediated targeting of
112 *Ptk2* led, as expected, to NPE cells devoid of FAK protein (FAK -/-) (Figure 1C). We re-
113 expressed FAK (FAK Rx) in otherwise FAK-deficient cells (FAK -/-) to levels comparable to
114 the wild-type NPE cells to enable direct comparison of cell clones that differ only in expression

115 of FAK (Figure 1C). To characterise the effects of deleting FAK on cellular phenotypes, we
116 first measured cell viability of FAK Rx or FAK -/- cells cultured for 3 days and found that FAK-
117 /- cells had significantly lower cell viability (Figure 1D). The loss of FAK also resulted in
118 profound morphological changes. Cells expressing FAK were well attached to the cell culture
119 substrate and displayed a spread and elongated mesenchymal-like morphology, while their
120 comparable FAK -/- cells adopted a more rounded and less spread morphology. Moreover,
121 FAK-deficient cells clustered tightly together with a more epithelial-like morphology and
122 displayed reduced contact with the substratum. They displayed increased junctional F-actin at
123 cell-cell contacts as a result of general remodelling of the actin and tubulin cytoskeletons
124 (Figure 1E). The expression of FAK was associated with a significant enrichment of the gene
125 set hallmark 'epithelial to mesenchymal transition' (FDR= 0.074) (Figure 1F). Consistent with
126 these changes, the depletion of FAK suppressed migration speed of NPE cells in 2-
127 dimentional (2D) culture and reduced the distance of 3-dimentional (3D) invasion into Matrigel,
128 respectively (Figures 1G and H).

129

130 **FAK promotes glycolysis and the TCA cycle in GBM mouse stem cells.**

131 In addition to the morphological and migratory phenotypes for which FAK is known to be
132 crucial, we made the observation that FAK Rx culture media, containing the pH indicator
133 phenol red, was consistently more yellow (acidic) compared to that of FAK -/- media leading
134 us to hypothesize that FAK may also regulate cellular metabolism (Figure S1A). To test this,
135 we performed a Seahorse XF Cell Mito Stress assay and found that FAK loss reduced both
136 extracellular acidification rate (ECAR), a surrogate measure of glycolytic flux, and reduced
137 oxygen consumption rate (OCR), a measure of mitochondrial function and health (Figure 2A
138 and B). This suggests that FAK loss has dampened the two main catabolic pathways
139 glycolysis and mitochondria OXPHOS. This led FAK -/- cells to be energetically supressed
140 and tending towards quiescence (Figure 2C). We found that spare respiration capacity,
141 maximal respiration and respiration-linked ATP production were significantly reduced in FAK

142 -/- cells when compared to FAK Rx cells (Figure 2D). Consistent with this, cellular metabolite
143 profiling revealed that FAK loss reduced glycolytic intermediates, TCA cycle metabolites, ATP
144 and its precursors (Figure 2E). In keeping with the observed metabolic effects, KEGG
145 metabolic pathway enrichment analysis of 132 cellular metabolites supported the regulation
146 of glycolysis, gluconeogenesis and TCA cycle in a FAK-dependent manner (Figure 2F).

147 To further characterise FAK's role in regulating glycolysis and the TCA cycle, we performed
148 stable isotope-labelled $^{13}C_6$-glucose tracing in FAK-expressing and FAK-deficient cells. We
149 found significantly reduced labelling of glycolytic intermediates within cells and of secreted
150 lactate, the end product of anaerobic glycolysis, in the absence of FAK (Figure 2G). We also
151 traced $^{13}C_5$-glutamine and found reduced labelling in most TCA cycle metabolites in FAK -/-
152 cells compared to FAK Rx cells (Figure 2H), indicative of a role for FAK in efficient glutamine
153 utilization. Taken together, these findings have uncovered a previously unknown role for FAK
154 in promoting both efficient glycolysis and the TCA cycle.

155 We noted that FAK's role in promoting glycolysis was consistently associated with higher
156 levels of glucose transporter proteins, namely Glucose transporter 1 (GLUT1, encoded by the
157 *Slc2a1* gene) and Glucose transporter 3 (GLUT 3, encoded by *Slc2a3* gene) (Figure S1B and
158 C), although we have not addressed causality of these changes.

159 **FAK regulates the length of mitochondria**

160 Previous studies have suggested that the shape of mitochondria is linked to their function, and
161 is responsive to nutrients and energy demands (reviewed in [20]). Specifically, it is proposed
162 that elongated mitochondria are associated with efficient OXPHOS [21–23]. Given this, and FAK's
163 role in regulating cell adhesion and cytoskeletal structure in the NPE model of GBM we have
164 used here, we asked whether FAK's regulation of the TCA cycle may be functionally linked to
165 FAK-dependent control of mitochondria morphology. We used Spinning disk super-resolution
166 by Optical pixel Reassignment (SoRa) microscopy to image the mitochondrial network stained
167 with MitoTracker (Figure 3A). We then used mitochondria features extraction tool (called

168 Mitochondria Analyser Fiji/ImageJ plugin[24,25]) to define the mitochondrial network and extract
169 different mitochondria features. This revealed that FAK's loss decreased the mitochondria
170 mean branch length (Figure 3B), implying that FAK promotes elongated and filamentous
171 mitochondria; a morphology associated with more efficient OXPHOS (Figure 2B, D and H).

172 **FAK regulates length of mitochondria via ROCK**

173 The shape and function of mitochondria is responsive to mechanical signals stimulated by
174 interaction with the ECM [8,10]. FAK is implicated in mechanotransduction by connecting signals
175 from the integrin family of ECM adhesion receptors to the actin cytoskeleton and actomyosin
176 contractility[26], and this has been shown to regulate the switch between epithelial- and
177 mesenchymal-like colon cancer cells[27]. Since the mesenchymal-like phenotype of the
178 transformed NPE cells we used here was also FAK-dependent (Figure 1E and F), we next
179 addressed whether FAK regulates mechanotransduction in NPE cells and, if so, whether this
180 is associated with changes in mitochondrial morphology and metabolism.

181 Phosphorylation of the regulatory light chain of myosin type II at serine(S)19 (hereafter p-
182 MLC(S19)), initiates actin-myosin interactions and assembles myosin filaments driving
183 actomyosin contractility[28]. We therefore used pMLC2(S19) as a surrogate measure of cellular
184 actomyosin contractility. In order to localise pMLC2(S19) at a subcellular level in FAK-
185 expressing and FAK-deficient cells, we used SoRa super-resolution microscopy and
186 quantified pMLC2(S19) intensity at cell-cell contacts, cell edge and cytoplasmic locales. We
187 found that FAK -/- cells had higher mean intensity of pMLC2(S19) at all of these subcellular
188 locales, while noting that pMLC2(S19) mean intensity was the highest at cell-cell contacts with
189 intense junctional F-actin (Figure 4A and B). This implied that the increased cell-cell contacts
190 formed as a result of FAK depletion were associated with highly localised F-actin and acto-
191 myosin contractility at the intercellular junctions. Next, we used inhibitors of ROCK, the kinase
192 the maintains MLC2(S19) phosphorylation[29]. We treated FAK -/- cells with 2 μM of the ROCK
193 inhibitor GSK269962A which reduced pMLC2 (S19) signal across the cells and induced cell
194 spreading, suppressing cell-cell contacts and restoring a mesenchymal-like morphology

195 (Figure 4A and B). Taken together, these data demonstrate that pMLC2(S19), and so by
196 inference actomyosin contractility, concentrates at cell-cell contacts in FAK-deficient cells and
197 that treating the cells with a ROCK inhibitor suppresses cell-cell contacts, enhances cell
198 spreading and restoration of the mesenchymal-like morphology typical of FAK-expressing
199 NPE cells.

200 Next, to address whether FAK's regulation of mitochondrial morphology may also be
201 dependent on its role in mechanotransduction, we used SoRa super-resolution microscopy to
202 characterise mitochondria morphology. We found that treating FAK-deficient cells with ROCK
203 inhibitors GSK269962A (2 μM) or Y27632 (20 μM) restored mitochondria morphology to that
204 exhibited by FAK-expressing cells, as judged by increased mitochondrial mean branch length
205 (Figure 4C and D and Figure S2A and B). This implies that inhibiting ROCK-pMLC(S19)
206 signalling enhances mitochondria elongation, linking FAK-mediated actomyosin contractility
207 to mitochondrial morphology.

208 **ROCK inhibitors increase TCA cycle activity and cell viability in FAK -/- cells.**

209 We hypothesized that the observed restitution of mitochondrial morphology might be
210 associated with the restoration of normal TCA cycle activity found by re-expressing FAK in
211 otherwise FAK-deficient cells. To test this, we analysed glutamine flux by performing a $^{13}C_5$
212 labelled glutamine tracer analysis of the TCA cycle metabolites and found that both ROCK
213 inhibitors GSK269962A (2 μM) and Y27632 (20 μM) increased glutamine utilisation to normal
214 levels (Figure 5A and Figure S3A). Together, these data imply that FAK regulates
215 mitochondrial morphology and TCA cycle activity by counteracting the ROCK-pMLC2(S19)
216 signalling axis. We found that restoration of TCA cycle activity by ROCK inhibitor treatment
217 rescued the loss of viability we observed in FAK-deficient cells (Figure 1D; Figure 5B). These
218 data indicate that FAK mediated suppression of the ROCK/p-MLC2(S19) pathway and
219 actomyosin contractility not only control maintenance of the mesenchymal-like morphology
220 and migration/invasion, but are also inextricably linked to mitochondrial morphology, cell
221 energy production and cell viability.

222 **FAK controls invasion, proliferation and survival in vivo**

223 Loss of FAK led to a significant decline in key hallmarks of the malignant phenotype in the
224 transformed neural stem cell model of GBM we used here, causing them to exhibit reduced
225 invasion, migration, cell viability and suppressed glycolysis and mitochondria function
226 rendering cells less energetic in vitro. To investigate whether this would translate to beneficial
227 properties in vivo, we performed an intracranial transplantation of GFP and luciferase-
228 expressing FAK -/- cells or FAK-Rx cells into the right-side brain hemisphere of CD1 nude
229 mice. We found that mice injected with cells lacking FAK had a significantly increased overall
230 survival (Figure 6A). CD1-nude mice with intracranial tumours formed after injecting FAK Rx
231 cells showed higher total body flux of the luciferase reporter when compared to FAK -/-
232 tumours at day 7 and day 17 (Figure 5B), suggesting that FAK expression increases tumour
233 growth. This was associated with a higher percentage of Ki67-expressing cells in sections of
234 FAK-expressing intracranial tumours at 17 days (Figure 6C and D). Moreover, FAK loss
235 significantly reduced the distance NPE cells could invade into the healthy brain tissue from
236 the tumour margin, a measure of their in vivo invasive capacity, implying a role for FAK in
237 cancer cells invasion in vivo (Figure 6E).

238 Finally, to investigate the relevance of our findings to human GBM, we used data from the
239 Cancer Genome Atlas (TCGA) to examine whether there was an association between FAK
240 protein levels (measured by Reverse Phase Protein Array) and patient survival in adult GBM
241 cases. We identified a group of patients with high (n=50) or low (n=48) FAK expression,
242 representing those with higher and lower quartile FAK expression, respectively. Our analysis
243 revealed an inverse correlation between FAK protein levels and overall patient survival (p =
244 0.0088), consistent with FAK contributing to GBM pathogenesis in patients (Figure 6F).

245

246

247

248 **Discussion**

249 Metabolic processes play critical roles in GBM as highlighted by the recently identified
250 metabolic subtypes with associated metabolic vulnerabilities[7,30]. Moreover, many GBM driver
251 mutations, such as loss of the tumour suppressor *PTEN*, or amplification of the genes for
252 receptor tyrosine kinase such as *EGFR* or platelet-derived growth factor receptor A (*PDGFRA*)
253 can enhance PI3K-AKT-mTOR signalling that, in turn, confers metabolic plasticity, enabling
254 GBM to tailor different metabolic pathways to their requirements [31]. Aerobic glycolysis has
255 been established as a metabolic pathway beneficial for tumour growth, and more recently the
256 TCA cycle has also been shown as important for cancer cells both in mouse models and
257 patients [32,33]. The role of the ECM in modulating these pathways to enhance metabolic
258 plasticity and resilience, including under therapeutic and mechanical stress, is beginning to be
259 elucidated and is cell-type and tissue specific. [8,10,34,35]. For example, mechanical cues from
260 the ECM influence ATP production and recycling, aiding the invasive migration of pancreatic
261 cancer cells[10]. In addition, increased stiffness boosts glycolysis in human bronchial epithelial
262 cells (HBECs), while transformed non-small cell lung cancer cells maintain high glycolytic rates
263 despite changes in environmental mechanics [9], demonstrating cell- and tumour-context
264 dependency. Furthermore, cell-ECM-mediated mechano-sensing and downstream signalling
265 are also known to regulate mitochondrial structure and function, conferring resilience to redox
266 stress in malignant human mammary epithelial cells[8].

267

268 Despite these advances, how specific adhesion proteins that function downstream of ECM-
269 cell interactions influence cellular energetics and metabolic flexibility is still unclear. The work
270 we present here has uncovered a novel link by which a pivotal adhesion protein, namely FAK,
271 is vital for optimal throughput of both glycolysis and the TCA cycle to ensure transformed
272 neural stem cells have sufficient energy production. When the gene encoding FAK is deleted,
273 the cellular energy production is significantly impaired and glutamine utilisation by the TCA
274 cycle is supressed. This is mediated by spatial regulation of actomyosin contractility, as

275 evidenced by activation of MLC2, likely via ROCK, including at cell-cell junctional contacts in
276 FAK depleted cells induced to undergo a mesenchymal-like to epithelial-like morphological
277 transition. This is important because glutamine is the major molecule that replenishes the TCA
278 cycle in glioma cell lines and its uptake is highly enhanced with minimal uptake in the
279 surrounding brain tissue in both mice and in patients [36].
280
281 In addition to the suppression of cellular energetics as a result of impaired glycolysis and TCA
282 cycle in FAK depleted transformed neural stem cells, we found visible changes to
283 mitochondrial morphology. Mitochondrial function is known to be closely connected to their
284 structure, which can have impact in human health and disease in a context dependent manner
285 [37]. We found that FAK's role in promoting mitochondria function was associated with an
286 elongated mitochondrial network. The changes in mitochondria morphology when FAK was
287 depleted was dependent on FAK-mediated suppression of signalling to p-MLC2. Indeed,
288 treating FAK-deficient cells with two distinct ROCK inhibitors (GSK269962A and Y27632)
289 restored mitochondria morphology to the elongated form that was associated with increased
290 glutamine incorporation into TCA cycle. In keeping with this, RhoA activity has been shown
291 to promote mitochondrial fission in cardiomyocytes by phosphorylating the protein Drp1 at
292 serine-616, leading to its re-localization to mitochondria[38], and this is blocked by treatment
293 with the ROCK inhibitor Y-27632 [38]. Additionally, higher Myosin II activity is associated with
294 mitochondria fragmentation in human melanoma cells [35]. We have concluded that one of
295 FAK's key roles in the GBM stem cell model is to sustain cellular energetics via both glycolysis
296 and the TCA cycle, linked to mitochondrial structural changes. We propose this contributes
297 to the impaired tumour growth and overall survival in vivo when cells are implanted into brains
298 of recipient mice.
299 As mentioned, the work we report here used a mesenchymal-like GBM stem cell model; when
300 we convert these into more epithelial-like cells by deletion of the gene encoding FAK, both
301 glycolysis and the TCA cycle are significantly impaired. However, previous studies in a
302 pancreatic ductal adenocarcinoma (PDAC) epithelial cell line and in epithelial-like GBM cell

303 lines, both cultured in serum-containing media, rather than the serum-free stem cell medium
304 we used here, suggests that FAK promotes glycolysis but suppresses OXPHOS under these
305 conditions[39,40]. Taken together, FAK's role in modulating metabolism in epithelial-like cells
306 differs from its role in mesenchymal-like cells of the same origin. In this regard, we note that
307 genome-wide CRISPR screens identified FAK as a fitness gene in the transcriptionally-defined
308 'injury response' GBM stem cell subtype but not in those defined as the 'developmental' GBM
309 stem cell subtype [15,16]. Injury response GBM stem cells map to the mesenchymal-like and
310 glycolytic/plurimetabolic cell states, while the developmental GBM stem cells, which are much
311 less dependent on integrin signalling and FAK, map to non-mesenchymal-like cell states, such
312 as 'neural precursor', 'astrocytic' and 'oligodendrocyte progenitor'-like[15,16]. Our data imply that
313 mesenchymal-like cells are dependent on FAK for energy production.

314 Our findings offer one possible explanation for why the genes encoding FAK, and other
315 integrin or their effector adhesion proteins, are amongst the primary 'fitness genes' identified
316 in drop-out screens in the highly treatment-resistant mesenchymal-like subtypes/GBM cell
317 states[15,16]. The novel role we have identified for FAK specifically in promoting metabolic
318 pathways in mesenchymal-like cells implies that FAK controls the bioenergetic and
319 biosynthetic requirements for the metabolic flexibility that characterises these GBM tumours.
320 In turn, this likely contributes to their growth in vivo and resistance to multiple therapeutics[41].
321 Our data imply that targeting FAK is likely to limit cellular energy production and metabolic
322 flexibility of mesenchymal-like and glycolytic/plurimetabolic GBM tumours. We therefore
323 suggest that a combination of targeting FAK together and other metabolic dependencies
324 identified in individual GBM subtypes may lead to synthetic lethality. Our future work will
325 address this as a potential therapeutic strategy.

326

327

328

329 **Methods**

330 **Experimental model and subject details**

331 **Cell culture**

332 NPE cells were generated using CRISPR/Cas9 mutagenesis from neural stem cells of adult
333 male C57BL/6-SCRM mice, as previously described[17]. NPE cells were maintained in 5%
334 CO_2 at 37 °C and were routinely tested for mycoplasma. Cell numbers were obtained using
335 the Countess automated cell counter (Thermo Fisher Scientific) by Trypan blue exclusion.
336 NPE cells were cultured in Dulbecco's Modified Eagle Medium and Ham's Nutrient Mixture
337 F12 (DMEM/F12; Sigma-Aldrich, #D8437) supplemented with 1.45 g/L D-Glucose (Sigma-
338 Aldrich, #G8644), 120 µg/mL bovine serum albumin (BSA) fraction V solution (Gibco, #15260-
339 037), 100 µM β-mercaptoethanol (Gibco; #31350-010), 1X MEM non-essential amino acid
340 (MEM-NEAA) solution (Gibco; #11140-035), 0.5X B-27 (Gibco; #17504-044) supplement,
341 0.5X N-2 supplement (Gibco; #15140-122), 10 ng/mL murine EGF (Peprotech; #315-09),
342 10 ng/mL human b-FGF (Peprotech; #100-18b), and 1 µg/mL laminin-I (R&D Systems; #3446-
343 005-01). Cells were passaged every second day by dissociation with Accutase (Sigma-
344 Aldrich; #A6964).

345 **Murine GBM model**

346 All treatments and procedures with mice were performed in accordance with protocols
347 approved by Home Office UK guidelines in a designated facility under a project license
348 PP7510272 held by V.B. at the University of Edinburgh. Up to 6 mice were caged in ventilated
349 cages in a pathogen-free facility on a 12-hour light/dark cycle with unlimited access to food
350 and water. 6–15-week-old female CD-1 nude mice (Charles River, Strain number 086) were
351 injected intracranially with 10,000 cells of either NPE-derived FAK-/- cells or NPE-derived FAK
352 Rx cells suspended in 2µl neural stem cell medium following administration of isoflurane
353 general anaesthesia. Mice were given analgesic buprenorphine subcutaneously during

354 surgery and the analgesic carprofen was administered in drinking water for 48 hours post-
355 surgery. Experimental mice were placed in a 25-30ºC heat box during recovery from
356 anaesthesia. Intracranial injections were performed in the mouse striatum at coordinates 0.6
357 mm anterior and 1.5 mm lateral to the bregma and 2.4 mm deep. Cells were prepared as
358 previously described[42]. Bioluminescent imaging was performed while mice were under
359 anaesthesia twice weekly by subcutaneous injection of 150 mg/kg luciferase using an IVIS
360 Lumina S5 system (Revvity) for monitoring tumour growth. For survival experiments, mice
361 were sacrificed by cervical dislocation upon the development of symptoms indicating the
362 presence of a brain tumour such as lethargy, instability, hunched posture and weight loss or
363 until a maximum time-point of 90 days post-injection. For endpoint experiments, mice were
364 sacrificed by cervical dislocation 17 days after cell implantation. Brains were collected
365 immediately after sacrifice and fixed in 10% Neutral Buffered Formalin (Merck; HT501128-4L)
366 overnight.

367 **Method details**

368 **Cell Treatments**

369 NPE cells were transfected by electroporation using a Lonza® Nucleofector™ 2b device and
370 the Lonza® Mouse Neural Stem Cell Nucleofector™ Kit (Lonza; #VPG-1004) according to the
371 manufacturer's instructions using the T-030 pulse code.

372 **Plasmids**

373 Plasmids for CRISPR/Cas9-mediated *Ptk2* knockout were generated by cloning
374 oligonucleotides encoding 1 sgRNAs targeting the *Ptk2* gene (Table S1) between the BbsI
375 sites of the pSpCas9(BB)-2A-GFP (PX458) plasmid [43] (a gift from Feng Zhang (Addgene
376 plasmid # 48138; RRID:Addgene_48138)). For *Ptk2* re-expression, total RNA was extracted
377 from NPE cells and reverse-transcribed to produce a cDNA library according to the
378 manufacturer's protocols (Qiagen; #74104 and Thermo Scientific; #K1621). The *Ptk2* gene

379 was amplified from the cDNA library using specific primers containing Kozak sequence[44]
380 before the start codon with 15 bp overhangs (L_*Ptk2*_HD and R_*Ptk2*_HD; Table S1) to
381 facilitate In-Fusion cloning (TakaraBio) into pQCXIN plasmid (a gift from Toby Hurd, Institute
382 of Genetics and Cancer, The University of Edinburgh) by In-Fusion cloning following the
383 manufacturer's instructions.

384 **CRISPR/Cas9 genome editing**

385 1 x 10^6 NPE cells were electroporated as described with 5 µg of either pSpCas9(BB)-2A-GFP
386 (PX458) with *Ptk2* sgRNA (sgRNA : 5'-GCAGTAGTGAGCCAACCACCT). This process was
387 repeated twice at 48 h intervals. Cells were suspended in 5% BSA (Merck; #12659) in PBS
388 and single cells were sorted using a BD FACSJazz™ cell sorter into wells of a 96-well cell
389 culture plate. Cells were incubated in a humidified 37°C incubator at 5% CO_2 until visible
390 colonies were formed. Colonies were passaged into two wells of a 6-well plate, one of which
391 was lysed directly in Laemmi buffer (50 mM Tris-HCl pH 6.8, 10% glycerol, 5% SDS, 5% β-
392 mercaptoethanol, bromophenol blue), and processed for western blotting to screen for FAK
393 depletion. Where FAK loss was detected, the remaining cells were passaged for further use.

394 **DNA construct expression**

395 For re-expression of the *Ptk2* gene in NPE FAK -/- cells, 2 x 10^6 cells were electroporated with
396 8 µg of FAK-pQCXIN. 48 h later, FAK-expressing cells were selected by addition of 0.5 mg/mL
397 G418 (Merck; #A1720). G418 selection was continued for 2 weeks to select only cells that had
398 stably integrated the FAK-pQCXIN construct. Expression of FAK in G418-selected cells was
399 confirmed by Western blotting. Selection was repeated every 3 months to ensure that the
400 population retained FAK expression.

401 **Cell lysis and western blotting**

402 Cells were washed once with cold PBS and lysed in cold RIPA buffer (150 mM NaCl, 50 mM
403 Tris-HCl pH 8, 1% v/v Triton X-100, 0.5% w/v sodium deoxycholate, 0.1% w/v sodium dodecyl
404 sulphate) supplemented with cOmplete™ ULTRA Protease Inhibitor (Roche; #5892953001)
405 and PhosSTOP™ Phosphatase Inhibitor (Roche; #4906845001) cocktail tablets for
406 15 minutes at 4 °C with gentle agitation. Crude extracts were collected into microcentrifuge
407 tubes and centrifuged at 4 °C for 15 minutes at 19,000 x *g*. Protein content was quantified
408 using the Pierce™ BCA assay kit (Thermo Scientific; #23225) according to the manufacturer's
409 protocol. 20 µg protein was diluted in Invitrogen novex NuPAGE LDS Sample Buffer (4X) and
410 heated to 95 °C for 7 minutes. Proteins were resolved by SDS-polyacrylamide gel
411 electrophoresis using 4-15% Mini-PROTEAN® TGX™ gels (BioRad; #4561086) and
412 transferred to PVDF membranes (BioRad; #1704157) using the Trans-Blot Turbo semi-dry
413 transfer system. Membranes were blocked by incubation with Tris-buffered saline (TBS)
414 supplemented with 5% BSA and 0.1% TWEEN® 20 (Millipore; #11332465001) (TBS-T) for 1
415 hour at room temperature with gentle agitation. Primary antibodies were diluted in TBS-T
416 supplemented with 5% BSA and incubated with membranes overnight at 4 °C with gentle
417 agitation. Membranes were washed 3 times with TBS-T at room temperature for 15 minutes
418 with agitation. Secondary antibodies were diluted in TBS-T supplemented with 5% BSA and
419 incubated with membranes for 45 min at room temperature with agitation. Membranes were
420 washed a further 3 times in TBS-T and bound antibodies were visualised using the Clarity
421 Western ECL substrate (BioRad; #1705061) with a ChemiDoc MP system (BioRad). Images
422 were collected and quantified using the BioRad ImageLab software (v6.1).

423 **In vitro 2D migration assay**

424 500 cells/well were plated into an IncuCyte® ImageLock 96-well plate (Sartorius; #BA-04856)
425 and imaged using a 10X objective every 10 min for a period of 48 h. Single-cell tracking was
426 performed in Fiji/ImageJ (v2.14.0/1.54f)[25] using Trackmate7 plugin[45].

427 **In vitro respirometry**

428 7000 cells/well were seeded in a Sea horse XF24 cell culture microplate for 48 hours (Part #
429 102342-100) after which medium was replaced with Seahorse XF medium (#103680-100)

430 supplemented with 10mM Glucose (103577-100), 2mM Glutamine (103579-100), 1mM
431 pyruvate, 10 ng/mL murine EGF, and 10 ng/mL human b-FGF and incubated in a CO_2 free
432 incubator for 30 minutes before the assay. During respirometry, the following inhibitors were
433 sequentially added via injection ports; oligomycin (1μM final), FCCP (2μM final), and antimycin
434 A/rotenone (0.5 μM final) during (concentrated stock solutions solubilized in Seahorse XF
435 medium (#103680-100) for mitochondrial stress test compounds). XFe24 sensor cartridges
436 containing 1ml Seahorse XF Calibrant Solution/well were incubated for 16 hrs before the
437 assay in a CO2 free incubator. Measurements were performed using Seahorse XFe24
438 Analyzer (Agilent) and data visualised and pre-processed using the Wave software (v.2.6.3.5).
439 Cells were dissociated with Accutase (Sigma-Aldrich; #A6964) and counted after the assay.
440 Data was normalised to cell number. 'Non respiratory OCR' was defined as measurement 10
441 (ie the OCR remaining following complete respiratory block with antimycin/rotenone). 'Basal
442 respiration' was calculated by subtracting OCR at measurement 10, from OCR at
443 measurement 3 (the basal OCR). Other parameters were similarly derived by subtraction;
444 'Proton Leak' measurement 10 from 4, Maximal respiration measurement 10 from 7, 'Spare
445 respiratory capacity' measurement 3 from 7, ATP-linked respiration (ATP production)
446 measurement 4 from 3.

447 **Drug treatments**

448 For drug treatment, cells were incubated with the indicated doses of either Y-27632
449 dihydrochloride (Tocris; #1254), GSK269962A (Cayman Chemical; #19180), or 0.02% DMSO.
450 Drugs were solubilised in DMSO to a stock concentration of 10 mM.

451 **LC-MS metabolomics**

452 500,000 cells/well were seeded in a 6-well plate and cultured for 48 hours before metabolites
453 were extracted with a solvent mixture (50% methanol, 30% acetonitrile, 20% water v/v) on dry
454 ice for 15 minutes with agitation. The extraction solution was then centrifuged at 16,100 x g

455 for 10 minutes at 4°C. The supernatants stored at -75°C prior to LC-MS analysis. Plates were
456 left in fume hood to dry and protein quantification was performed using the Lowry assay.

457 Metabolites were analysed on a Dionex Ultimate 3000 UHPLC (Thermo Fisher Scientific)
458 coupled to a Q Exactive Hybrid Orbitrap MS (Thermo Fisher Scientific). Hydrophilic interaction
459 liquid chromatography (HILIC) using a ZIC-pHILIC analytical column (2.1 × 150 mm, SeQuant-
460 MerckMillipore) coupled with a guard column (2.1 × 20 mm) was used for chromatographic
461 separation of metabolites. A gradient using mobile phase A (20 mM ammonium carbonate,
462 0.01% (v/v) ammonium hydroxide), and B (acetonitrile) was used. The gradient was set from
463 95% to 5% B over 20 min and reequilibrated to initial conditions for 7 min. The flow rate was
464 200 ml/min, and the temperature was at 45°C. The injection volume was 5 µl. MS data was
465 acquired in positive/negative polarity switch mode in the m/z range of 70–900 Da, with a
466 resolving power of 70,000 (FWHM). Metabolites were identified by matching accurate mass
467 measurements (< 5 ppm) and retention times to an in-house library of standards. Skyline
468 21.2.0.568[46] was used to quantify the metabolites by integrating the area under the curve and
469 normalizing the values to total protein content. Metaboanalyst 5.0[47] was used to perform log
470 transformation (base 10), auto scaling (data mean-centred and divided by the standard
471 deviation of each variable) and KEGG metabolic pathway enrichment analysis.

472 **$^{13}C_6$-glucose and $^{13}C_5$-glutamine LC-MS metabolomics**

473 500,000 cells/well were seeded in a 6-well plate and cultured for 48 hours before media was
474 exchanged with media containing $^{13}C_6$-Glucose (Sigma Aldrich;389374) at 4.5 g/L and
475 incubated at 37°C for 1 hr for $^{13}C_6$-glucose tracing. For glutamine tracing media was replaced
476 with media containing $^{13}C_5$-glutamine (Sigma Aldrich; 605166) at 0.365 g/L and incubated at
477 37°C for 3 hr. Cells were washed twice with PBS and metabolites were extracted with a solvent
478 mixture (50% methanol, 30% acetonitrile, and 20% water (v/v)) on dry ice for 15 minutes with
479 agitation. The extraction solution was then centrifuged at 16,100 x g for 10 minutes at 4°C.
480 The supernatants were stored at -75°C prior to LC-MS analysis. Metabolites were analysed

481 as described above. Isotope natural abundance was corrected and % Enrichment of
482 isotopolouges was calculated using “accucor” package in R.

483 **Proteomics**

484 Cells were lysed with the PAC lysis buffer (5% SDS, 100 mM Tris pH 8.5, 1 mg/ml
485 chloroacetamide, 1.5 mg/ml Tris (2-carboxyethyl) phosphine), heated at 95 degrees for 30
486 minutes and then sonicated. Lysate was then added to a Kingfisher 96 well deep well plate
487 and prepared for an 8h digest protocol on the Kingfisher Duo. Lysate was added to Row G
488 with MagReSyn HILIC beads and acetonitrile is added to 70% final concentration. Rows D, E,
489 and F are filled with 95% acetonitrile and Rows B and C are filled with 70% ethanol. The digest
490 buffer (1 µg/ml MS grade trypsin in 50 mM Triethyammonium bicarbonate) is added to Row
491 A. Desalted peptides were then loaded onto 25cm Aurora Columns (IonOptiks, Australia)
492 using a RSLC nano uHPLC systems connected to a Fusion Lumos mass spectrometer.
493 Peptides were separated by a 70 min linear gradient from 5% to 30% acetonitrile, 0.5% acetic
494 acid. The mass spectrometer was operated in DIA mode, acquiring a MS 350-1650 Da at 120k
495 resolution followed by MS/MS on 45 windows with 0.5 Da overlap (200-2000 Da) at 30 k with
496 a NCE setting of 28. The output was analyzed on DIA-NN (v. 1.8.2 beta 27) with the Mus
497 musculus FASTA. The precursor m/z range was set to 350-1650 and the fragment ion range
498 was set to 200-2000. LFQ intensities for proteins quantified in at least three biological
499 replicates in at least one experimental group were binary-logarithm transformed. Missing
500 values were imputed from a width-compressed, down-shifted Gaussian distribution using
501 Perseus (version 1.6.15.0)[48].

502 **Immunofluorescence microscopy**

503 Coverslips were washed overnight in 1 M hydrochloric acid at 65 °C before being rinsed twice
504 with deionised water and stored in 70% ethanol. Prior to plating cells, coverslips were washed
505 in PBS and coated with 1 µg / mL laminin-I (R&D Systems; #3446-005-01) at 37 °C for 1
506 hour. 5×10^4 cells were plated on coated coverslips and allowed to adhere for 48 h. Cells

507 were fixed by replacing the media with fixing buffer (3.7% Formaldehyde / 100 mM PIPES /
508 10 mM EGTA / 1 mM MgCl2 / 0.2% v/v Triton X-100) and incubation at 37 °C for 15 min. Cells
509 were washed once with TBS and incubated in 0.1 M glycine (Sigma-Aldrich; #G8898) in TBS
510 for 10 minutes at room temperature to quench excess formaldehyde before an additional wash
511 with TBS. Permeabilisation was performed with TBS-T for 5 minutes at room temperature.
512 Cells were washed once in TBS supplemented with 0.05% Triton X-100 (v/v) and then blocked
513 with TBS supplemented with 2% BSA and 0.1% Triton X-100 (v/v) for 1 hour at room
514 temperature. Primary antibodies were diluted in blocking buffer and incubated with cells
515 overnight at 4 °C, followed by 3 washes with TBS-T for 5 minutes each at room temperature
516 with gentle agitation. Secondary antibodies and phalloidin-Atto647N (Sigma-Aldrich; #65906,
517 working concentration 25 nM) were diluted in blocking buffer and incubated with cells in the
518 dark for 45 minutes at room temperature. Cells were washed a further 3 times in the dark in
519 TBST at room temperature for 5 minutes each with gentle agitation, followed by a final wash
520 with deionised water. Cells were mounted with ProLong™ Glass Antifade Mountant with
521 NucBlue™ (Invitrogen; #P36981) for nuclear staining. Cells were imaged on Nicon CSU-W1
522 SoRa microscope using a 405, 488 nm, 568 nm and 647 nm lasers with 100X oil immersion
523 objective. Images were acquired using NIS-Elements AR 5.30.03 (Build 1549) or NIS-
524 Elements AR 6.10.01 (Build 2027) software. To acquire Z-stacks, 4 µm thickness from the cell
525 bottom were imaged with 0.1µm or 0.2µm step size. Images were denoised and deconvolved
526 using NIS-Elements AR 5.21.03 (Build 1489) or NIS-Elements AR 6.10.01 (Build 2027)
527 software and processed using Fiji/ImageJ (v2.14.0/1.54f)[25].

528 **MitoTracker staining**

529 MitoTracker deep red FM (Invitrogen; #M22426) was solubilized in DMSO at a stock
530 concentration of 100 µM and stored at -20°C in aliquots. MitoTracker stock solution was diluted
531 in media to a concentration of 400 nM which was added directly to cell culture media already
532 in the culture yielding a final concertation of 200 nM. After a 45 min incubation cells were fixed

533 and permeabilised as described above. Mitochondria analyser (v2.3.1) [24] was used in
534 Fiji/ImageJ (v2.14.0/1.54f)[25] to threshold and extract mitochondria network features from the
535 z-plane closest to the substratum, where well-resolved mitochondria were present.

536 **Immunohistochemistry**

537 Brain samples from mice were fixed in 10% Neutral Buffered Formalin for 16 hours and then
538 transferred to 70% ethanol. Brain samples were then cut into 4 coronal sections before
539 embedding in paraffin blocks. For each brain sample, 8 µm sections were prepared for
540 hematoxilin and eosin (H&E) staining. For immunohistochemistry staining, 8 µm sections were
541 mounted on glass slides. Paraffin removal from sections was achieved by washing samples
542 in xylene for 5 minutes twice. Sections were rehydrated by incubation in decreasing ethanol
543 solutions (100%, 75% and 50% ethanol) for 3 minutes each followed by a rinse in water. Tissue
544 sections were boiled for 5 minutes in 10 mM sodium citrate buffer (0.825 M sodium citrate,
545 0.175 M citric acid; pH 6.0) for antigen epitope retrieval. Sections were then rinsed in water
546 and washed in TBS-T twice for 5 minutes each. Sections were incubated with Dako REAL
547 peroxidase block solution (Agilent; #S2023) for 5 minutes and rinsed in water. For protein
548 block, sections were treated with serum-free protein block solution (Agilent; #X0909) for 10
549 minutes. Primary antibodies were prepared in antibody diluent (Agilent; #S3022) and
550 incubated with sections overnight at 4ºC. Sections were washed 3 times in TBS-T for 5
551 minutes each and incubated with DAKO EnVision-HRP rabbit/mouse (Agilent; #K5007) for 45
552 minutes at room temperature. Sections were washed 3 times in TBS-T for 5 minutes each and
553 developed with DAB-chromagen (Agilent; #K3468) at 1:50 dilution for 10 minutes followed by
554 a rinse in water. Sections were then immersed in Mayer´s Hematoxylin solution (Agilent;
555 #S3309) for 2 minutes at room temperature and rinsed in water before incubation with Scot´s
556 tap water solution (3.5 g/L sodium bicarbonate, 20 g/L magnesium sulphate) for 2 minutes and
557 a final rinse in water. Sections were dehydrated by incubation in ethanol solutions (50%, 75%
558 and 100% ethanol) for 3 minutes and washed in xylene twice for 5 minutes. Slides were

559 mounted with DPX mountant (Sigma-Aldrich; #06522). Images of stained sections were
560 obtained using a Nanozoomer slide scanner (Hamamatsu Photonics). Ki67 and GFP
561 staining's were analysed using QuPath software (version 4.0.3). GFP staining was used to
562 distinguish tumour regions.

563 **Antibodies**

564 Antibodies used for western blotting were anti-FAK (Cell Signaling Technology; #3285,
565 1:1000), anti-Phospho-FAK (Tyr397) (Cell Signalling Technology; #3283, 1:1000), anti-NF1
566 (Bethyl; #A300-140A, 1:2000), anti-PTEN (Cell Signalling Technology; #9559, 1:1000), anti-
567 EGFR (Cell Signalling Technology; #4267, 1:1000), anti-COXIV (Cell Signaling Technology;
568 #4850, 1:1000), anti- COFILIN (Cell Signaling Technology; #5175, 1:1000), anti-Glut1 (Cell
569 Signalling Technology;# 73015, 1:1000), anti-Enolase 2 (Cell Signaling Technology; #24330,
570 1:1000). Primary antibodies used for immunofluorescence microscopy were anti-α-Tubulin
571 (Cell Signalling Technology; #3873, 1:1000), and anti-Myosin Light Chain 2, phospho (Ser19)
572 (Cell Signalling Technology; # 3675, 1:200). Secondary antibodies used for
573 immunofluorescence Alexa Fluor™ 568-conjugated anti-mouse IgG (Invitrogen; #A-11004, all
574 1:400). Antibodies used for immunohistochemistry were anti-GFP (ChromoTek; # PABG1-20;
575 1:100) and anti-Ki67 (Cell Signalling Technology; #12202, 1:1000).
576

577 **Overall survival of GBM patients:**

578 GBM patient survival data was correlated with FAK protein expression (RPPA data) using data
579 from the GBM TCGA database[50] which was accessed through cBioPortal[51–53]. GBM patients
580 were segregated into two groups according to FAK protein levels. FAK-high and FAK-low
581 groups representing patients with upper (n=50) and lower quartile (n=48) FAK protein
582 expression levels, respectively.

583 **Computational methods**

584 Where R packages were used for analysis, this was performed using R (v4.4.1). Data were
585 plotted using GraphPad Prism 9 (v9.4.0), R packages; gplots (v3.2.0)[54], ggplot2[55], and
586 RColorBrewer[56]. $^{13}C_6$-glucose and $^{13}C_5$-glutamine isotope tracing data were plotted using
587 Escher-Trace [57].

588 **Quantification and statistical analysis**

589 Figure legends contain biological and technical replicate information. Plots include each data
590 point, mean and SD, or mean and SEM. Statistical analyses were performed in GraphPad
591 Prism 9 (v9.4.0) or R (v4.4.1) or Metaboanalyst 5.0[47]. GSEA analysis was performed using
592 the GSEA software (v4.3.1)[58]. *P*-values are represented
593 as $^{*}P < 0.05$; $^{**}P < 0.01$; $^{***}P < 0.005$; $^{****}P < 0.001$, between the indicated groups.

594 **Acknowledgments**

595 We acknowledge Ann Wheeler, Laura Murphy, James Iremonger and Matthew Pearson of the
596 Advanced Imaging Resource at the Institute of Genetics and Cancer, University of Edinburgh,
597 for their support and expertise. We thank Thomas MacVicar of the The CRUK Scotland
598 Institute, Glasgow, for the insightful discussions. This work was funded by a Cancer Research
599 UK Programme grant award (C157/A24837) to V.G.B. and M.C.F., a joint Brain Tumour Award
600 from Cancer Research UK (C42454/A28596) and The Brain Tumour Charity award (GN-
601 000676) to N.O.C. and M.C.F., and a Cancer Research UK award (A28592) to S.M.P.

602 **Author contributions**

603 M.C.F. and V.G.B. conceived and co-ordinated the project and helped to design and interpret
604 experiments. R.H.A.M., J.C.D., V.A.G., V.G.B., and M.C.F. designed the experiments.
605 R.H.A.M., J.C.D., V.A.G., A.V.K., J.M.J., G.H., V.G.B., and M.C.F. interpreted the results.
606 R.H.A.M., J.C.D., V.A.G., M.T.M., R.N.C., C.D. performed the experiments. M.C.F., V.G.B.,
607 S.M.P., N.O.C. and R.H.A.M. contributed to supervision. R.H.A.M., J.C.D., V.A.G. and C.P.

608 analyzed the data. R.H.A.M prepared figures. R.H.A.M, J.C.D., and M.C.F. wrote the paper.

609 All authors read and approved the manuscript.

610 **Declaration of interests**

611 The authors declare no competing interests.

612 **References**

613 1. Noroxe, D.S., Poulsen, H.S., and Lassen, U. (2016). Hallmarks of glioblastoma: a systematic
614 review. ESMO Open *1*, 144. https://doi.org/10.1136/ESMOOPEN-2016-000144.

615 2. Osuka, S., and Van Meir, E.G. (2017). Overcoming therapeutic resistance in glioblastoma: the
616 way forward. J Clin Invest *127*, 415–426. https://doi.org/10.1172/JCI89587.

617 3. Singh, S.K., Hawkins, C., Clarke, I.D., Squire, J.A., Bayani, J., Hide, T., Henkelman, R.M.,
618 Cusimano, M.D., and Dirks, P.B. (2004). Identification of human brain tumour initiating cells.
619 Nature *432*, 396–401. https://doi.org/10.1038/NATURE03128.

620 4. Renoult, O., Laurent-Blond, M., Awada, H., Oliver, L., Joalland, N., Croyal, M., Paris, F., Gratas,
621 C., and Pecqueur, C. (2024). Metabolic profiling of glioblastoma stem cells reveals pyruvate
622 carboxylase as a critical survival factor and potential therapeutic target. Neuro Oncol *26*,
623 1572–1586. https://doi.org/10.1093/NEUONC/NOAE106.

624 5. Pelaz, S.G., Jaraíz-Rodríguez, M., Alvarez-V azquez, A., Talaver on, R., García-Vicente, L.,
625 Flores-Hern andez, R., omez de Cedr on, M.G., Tabernero, M., Ramírez de Molina, A., on Lillo,
626 C., et al. (2017). Targeting metabolic plasticity in glioma stem cells in vitro and in vivo through
627 specific inhibition of c-Src by TAT-Cx43 266-283-NC-ND license
628 (http://creativecommons.org/licenses/by-nc-nd/4.0/). JSES Open Access *1*, 139–140.
629 https://doi.org/10.1016/j.ebiom.2020.103134.

630 6. Hanahan, D., and Weinberg, R.A. (2011). Hallmarks of cancer: The next generation. Cell *144*,
631 646–674. https://doi.org/10.1016/j.cell.2011.02.013.

632 7. Garofano, L., Migliozzi, S., Oh, Y.T., D'Angelo, F., Najac, R.D., Ko, A., Frangaj, B., Caruso, F.P.,
633 Yu, K., Yuan, J., et al. (2021). Pathway-based classification of glioblastoma uncovers a
634 mitochondrial subtype with therapeutic vulnerabilities. Nature Cancer 2020 2:2 *2*, 141–156.
635 https://doi.org/10.1038/s43018-020-00159-4.

636 8. Tharp, K.M., Higuchi-Sanabria, R., Timblin, G.A., Ford, B., Garzon-Coral, C., Schneider, C.,
637 Muncie, J.M., Stashko, C., Daniele, J.R., Moore, A.S., et al. (2021). Adhesion-mediated
638 mechanosignaling forces mitohormesis. Cell Metab *33*, 1322-1341.e13.
639 https://doi.org/10.1016/J.CMET.2021.04.017.

640 9. Park, J.S., Burckhardt, C.J., Lazcano, R., Solis, L.M., Isogai, T., Li, L., Chen, C.S., Gao, B., Minna,
641 J.D., Bachoo, R., et al. (2020). Mechanical regulation of glycolysis via cytoskeleton
642 architecture. Nature 2020 578:7796 *578*, 621–626. https://doi.org/10.1038/s41586-020-
643 1998-1.

644 10. Papalazarou, V., Zhang, T., Paul, N.R., Juin, A., Cantini, M., Maddocks, O.D.K., Salmeron-
645 Sanchez, M., and Machesky, L.M. (2020). The creatine–phosphagen system is
646 mechanoresponsive in pancreatic adenocarcinoma and fuels invasion and metastasis. Nature
647 Metabolism 2020 2:1 *2*, 62–80. https://doi.org/10.1038/s42255-019-0159-z.

648 11. DeWane, G., Salvi, A.M., and DeMali, K.A. (2021). Fueling the cytoskeleton-links between cell
649 metabolism and actin remodeling. J Cell Sci *134*.
650 https://doi.org/10.1242/JCS.248385/237339.

651 12. Frame, M.C., Patel, H., Serrels, B., Lietha, D., and Eck, M.J. (2010). The FERM domain:
652 organizing the structure and function of FAK. Nat Rev Mol Cell Biol *11*, 802–814.
653 https://doi.org/10.1038/NRM2996.

654 13. Horton, E.R., Byron, A., Askari, J.A., Ng, D.H.J., Millon-Frémillon, A., Robertson, J., Koper, E.J.,
655 Paul, N.R., Warwood, S., Knight, D., et al. (2015). Definition of a consensus integrin adhesome
656 and its dynamics during adhesion complex assembly and disassembly. Nature Cell Biology
657 2015 17:12 *17*, 1577–1587. https://doi.org/10.1038/ncb3257.

658 14. Dawson, J.C., Serrels, A., Stupack, D.G., Schlaepfer, D.D., and Frame, M.C. (2021). Targeting
659 FAK in anticancer combination therapies. Nature Reviews Cancer 2021 21:5 *21*, 313–324.
660 https://doi.org/10.1038/s41568-021-00340-6.

661 15. Richards, L.M., Whitley, O.K.N., MacLeod, G., Cavalli, F.M.G., Coutinho, F.J., Jaramillo, J.E.,
662 Svergun, N., Riverin, M., Croucher, D.C., Kushida, M., et al. (2021). Gradient of Developmental
663 and Injury Response transcriptional states defines functional vulnerabilities underpinning
664 glioblastoma heterogeneity. Nature Cancer 2021 2:2 *2*, 157–173.
665 https://doi.org/10.1038/s43018-020-00154-9.

666 16. MacLeod, G., Molaei, F., Haider, S., Almeida, M.P., Lin, S., Kushida, M., Sureshkumar, H.,
667 Bhatti, J.K., Lu, J.Q., Schramek, D., et al. (2024). Fitness Screens Map State-Specific
668 Glioblastoma Stem Cell Vulnerabilities. Cancer Res. https://doi.org/10.1158/0008-5472.CAN-
669 23-4024.

670 17. Gangoso, E., Southgate, B., Bradley, L., Rus, S., Galvez-Cancino, F., McGivern, N., Güç, E.,
671 Kapourani, C.A., Byron, A., Ferguson, K.M., et al. (2021). Glioblastomas acquire myeloid-
672 affiliated transcriptional programs via epigenetic immunoediting to elicit immune evasion.
673 Cell *184*, 2454-2470.e26. https://doi.org/10.1016/J.CELL.2021.03.023.

674 18. Loftus, A.E.P., Romano, M.S., Phuong, A.N., McKinnel, B.J., Muir, M.T., Furqan, M., Dawson,
675 J.C., Avalle, L., Douglas, A.T., Mort, R.L., et al. (2024). An ILK/STAT3 pathway controls
676 glioblastoma stem cell plasticity. Dev Cell. https://doi.org/10.1016/J.DEVCEL.2024.09.003.

677 19. Bao, S., Wu, Q., McLendon, R.E., Hao, Y., Shi, Q., Hjelmeland, A.B., Dewhirst, M.W., Bigner,
678 D.D., and Rich, J.N. (2006). Glioma stem cells promote radioresistance by preferential
679 activation of the DNA damage response. Nature 2006 444:7120 *444*, 756–760.
680 https://doi.org/10.1038/nature05236.

681 20. Chen, W., Zhao, H., and Li, Y. (2023). Mitochondrial dynamics in health and disease:
682 mechanisms and potential targets. Signal Transduct Target Ther *8*.
683 https://doi.org/10.1038/S41392-023-01547-9.

684 21. Yao, C.H., Wang, R., Wang, Y., Kung, C.P., Weber, J.D., and Patti, G.J. (2019). Mitochondrial
685 fusion supports increased oxidative phosphorylation during cell proliferation. Elife *8*.
686 https://doi.org/10.7554/ELIFE.41351.

687 22. Baek, M.L., Lee, J., Pendleton, K.E., Berner, M.J., Goff, E.B., Tan, L., Martinez, S.A., Mahmud,
688 I., Wang, T., Meyer, M.D., et al. (2023). Mitochondrial structure and function adaptation in
689 residual triple negative breast cancer cells surviving chemotherapy treatment. Oncogene *42*,
690 1117. https://doi.org/10.1038/S41388-023-02596-8.

691 23. Wang, Z., Tang, S., Cai, L., Wang, Q., Pan, D., Dong, Y., Zhou, H., Li, J., Ji, N., Zeng, X., et al.
692 (2024). DRP1 inhibition-mediated mitochondrial elongation abolishes cancer stemness,
693 enhances glutaminolysis, and drives ferroptosis in oral squamous cell carcinoma. British
694 Journal of Cancer 2024 130:11 *130*, 1744–1757. https://doi.org/10.1038/s41416-024-02670-
695 2.

696 24. Chaudhry, A., Shi, R., and Luciani, D.S. (2020). A pipeline for multidimensional confocal
697 analysis of mitochondrial morphology, function, and dynamics in pancreatic β-cells. Am J
698 Physiol Endocrinol Metab *318*, E87–E101.
699 https://doi.org/10.1152/AJPENDO.00457.2019/ASSET/IMAGES/LARGE/ZH10022082780008.J
700 PEG.

701 25. Schindelin, J., Arganda-Carreras, I., Frise, E., Kaynig, V., Longair, M., Pietzsch, T., Preibisch, S.,
702 Rueden, C., Saalfeld, S., Schmid, B., et al. (2012). Fiji - an Open Source platform for biological
703 image analysis. Nat Methods *9*, 10.1038/nmeth.2019. https://doi.org/10.1038/NMETH.2019.

704 26. Di, X., Gao, X., Peng, L., Ai, J., Jin, X., Qi, S., Li, H., Wang, K., and Luo, D. (2023). Cellular
705 mechanotransduction in health and diseases: from molecular mechanism to therapeutic
706 targets. Signal Transduction and Targeted Therapy 2023 8:1 *8*, 1–32.
707 https://doi.org/10.1038/s41392-023-01501-9.

708 27. Avizienyte, E., and Frame, M.C. (2005). Src and FAK signalling controls adhesion fate and the
709 epithelial-to-mesenchymal transition. Curr Opin Cell Biol *17*, 542–547.
710 https://doi.org/10.1016/J.CEB.2005.08.007.

711 28. Yu, H., Chakravorty, S., Song, W., and Ferenczi, M.A. (2016). Phosphorylation of the
712 regulatory light chain of myosin in striated muscle: methodological perspectives. European
713 Biophysics Journal 2016 45:8 *45*, 779–805. https://doi.org/10.1007/S00249-016-1128-Z.

714 29. Parsons, J.T., Horwitz, A.R., and Schwartz, M.A. (2010). Cell adhesion: integrating cytoskeletal
715 dynamics and cellular tension. Nat Rev Mol Cell Biol *11*, 633.
716 https://doi.org/10.1038/NRM2957.

717 30. Zhang, J., Sun, R., Lyu, Y., Liu, C., Liu, Y., Feng, Y., Fu, M., Wong, P.J.C., Du, Z., Qiu, T., et al.
718 (2024). Proteomic profiling of gliomas unveils immune and metabolism-driven subtypes with
719 implications for anti-nucleotide metabolism therapy. Nature Communications 2024 15:1 *15*,
720 1–15. https://doi.org/10.1038/s41467-024-54352-5.

721 31. Huse, J.T., and Holland, E.C. (2010). Targeting brain cancer: advances in the molecular
722 pathology of malignant glioma and medulloblastoma. Nature Reviews Cancer 2010 10:5 *10*,
723 319–331. https://doi.org/10.1038/nrc2818.

724 32. Heiden, M.G.V., Cantley, L.C., and Thompson, C.B. (2009). Understanding the warburg effect:
725 The metabolic requirements of cell proliferation. Science (1979) *324*, 1029–1033.

726 https://doi.org/10.1126/SCIENCE.1160809/ASSET/C00CA2CE-14F9-4352-AC43-
727 7D1BB04B41D8/ASSETS/GRAPHIC/324_1029_F4.JPEG.

728 33. Ward, P.S., and Thompson, C.B. (2012). Metabolic Reprogramming: A Cancer Hallmark Even
729 Warburg Did Not Anticipate. Cancer Cell *21*, 297–308.
730 https://doi.org/10.1016/J.CCR.2012.02.014/ASSET/AD6E4E9C-CAAE-44AD-B50D-
731 082550CB6DD7/MAIN.ASSETS/GR6.JPG.

732 34. Romani, P., Nirchio, N., Arboit, M., Barbieri, V., Tosi, A., Michielin, F., Shibuya, S., Benoist, T.,
733 Wu, D., Hindmarch, C.C.T., et al. (2022). Mitochondrial fission links ECM
734 mechanotransduction to metabolic redox homeostasis and metastatic chemotherapy
735 resistance. Nature Cell Biology 2022 24:2 *24*, 168–180. https://doi.org/10.1038/s41556-022-
736 00843-w.

737 35. Crosas-Molist, E., Graziani, V., Maiques, O., Pandya, P., Monger, J., Samain, R., George, S.L.,
738 Malik, S., Salise, J., Morales, V., et al. (2023). AMPK is a mechano-metabolic sensor linking cell
739 adhesion and mitochondrial dynamics to Myosin-dependent cell migration. Nature
740 Communications 2023 14:1 *14*, 1–22. https://doi.org/10.1038/s41467-023-38292-0.

741 36. Venneti, S., Dunphy, M.P., Zhang, H., Pitter, K.L., Zanzonico, P., Campos, C., Carlin, S.D., La
742 Rocca, G., Lyashchenko, S., Ploessl, K., et al. (2015). Glutamine-based PET imaging facilitates
743 enhanced metabolic evaluation of gliomas in vivo. Sci Transl Med *7*.
744 https://doi.org/10.1126/SCITRANSLMED.AAA1009/SUPPL_FILE/7-
745 274RA17_TABLES_S6_AND_S7.ZIP.

746 37. Sprenger, H.G., and Langer, T. (2019). The Good and the Bad of Mitochondrial Breakups.
747 Trends Cell Biol *29*, 888–900. https://doi.org/10.1016/J.TCB.2019.08.003.

748 38. Brand, C.S., Tan, V.P., Brown, J.H., and Miyamoto, S. (2018). RhoA regulates Drp1 mediated
749 mitochondrial fission through ROCK to protect cardiomyocytes. Cell Signal *50*, 48.
750 https://doi.org/10.1016/J.CELLSIG.2018.06.012.

751 39. Zhang, J., Gao, Q., Zhou, Y., Dier, U., Hempel, N., and Hochwald, S.N. (1926). Focal adhesion
752 kinase-promoted tumor glucose metabolism is associated with a shift of mitochondrial
753 respiration to glycolysis. Oncogene *35*, 1926–1942. https://doi.org/10.1038/onc.2015.256.

754 40. Che, P., Yu, L., Friedman, G.K., Wang, M., Ke, X., Wang, H., Zhang, W., Nabors, B., Ding, Q.,
755 and Han, X. (2021). Integrin αvβ3 Engagement Regulates Glucose Metabolism and Migration
756 through Focal Adhesion Kinase (FAK) and Protein Arginine Methyltransferase 5 (PRMT5) in
757 Glioblastoma Cells. Cancers (Basel) *13*, 1–16. https://doi.org/10.3390/CANCERS13051111.

758 41. Bhat, K.P.L., Balasubramaniyan, V., Vaillant, B., Ezhilarasan, R., Hummelink, K., Hollingsworth,
759 F., Wani, K., Heathcock, L., James, J.D., Goodman, L.D., et al. (2013). Mesenchymal
760 Differentiation Mediated by NF-κB Promotes Radiation Resistance in Glioblastoma. Cancer
761 Cell *24*, 331–346. https://doi.org/10.1016/J.CCR.2013.08.001.

762 42. Pollard, S.M., Yoshikawa, K., Clarke, I.D., Danovi, D., Stricker, S., Russell, R., Bayani, J., Head,
763 R., Lee, M., Bernstein, M., et al. (2009). Glioma Stem Cell Lines Expanded in Adherent Culture
764 Have Tumor-Specific Phenotypes and Are Suitable for Chemical and Genetic Screens. Cell
765 Stem Cell *4*, 568–580. https://doi.org/10.1016/J.STEM.2009.03.014.

43. Ran, F.A., Hsu, P.D., Wright, J., Agarwala, V., Scott, D.A., and Zhang, F. (2013). Genome engineering using the CRISPR-Cas9 system. Nat Protoc *8*, 2281–2308. https://doi.org/10.1038/NPROT.2013.143.

44. Kozak, M. (1987). An analysis of 5'-noncoding sequences from 699 vertebrate messenger RNAs. Nucleic Acids Res *15*, 8125–8148. https://doi.org/10.1093/NAR/15.20.8125.

45. Ershov, D., Phan, M.S., Pylvänäinen, J.W., Rigaud, S.U., Le Blanc, L., Charles-Orszag, A., Conway, J.R.W., Laine, R.F., Roy, N.H., Bonazzi, D., et al. (2022). TrackMate 7: integrating state-of-the-art segmentation algorithms into tracking pipelines. Nature Methods 2022 19:7 *19*, 829–832. https://doi.org/10.1038/s41592-022-01507-1.

46. Pino, L.K., Searle, B.C., Bollinger, J.G., Nunn, B., MacLean, B., and MacCoss, M.J. (2020). The Skyline ecosystem: Informatics for quantitative mass spectrometry proteomics. Mass Spectrom Rev *39*, 229–244. https://doi.org/10.1002/MAS.21540.

47. Xia, J., Psychogios, N., Young, N., and Wishart, D.S. (2009). MetaboAnalyst: a web server for metabolomic data analysis and interpretation. Nucleic Acids Res *37*, W652–W660. https://doi.org/10.1093/NAR/GKP356.

48. Tyanova, S., Temu, T., Sinitcyn, P., Carlson, A., Hein, M.Y., Geiger, T., Mann, M., and Cox, J. (2016). The Perseus computational platform for comprehensive analysis of (prote)omics data. Nat Methods *13*, 731–740. https://doi.org/10.1038/NMETH.3901.

49. Schindelin, J., Arganda-Carreras, I., Frise, E., Kaynig, V., Longair, M., Pietzsch, T., Preibisch, S., Rueden, C., Saalfeld, S., Schmid, B., et al. (2012). Fiji: an open-source platform for biological-image analysis. Nature Methods 2012 9:7 *9*, 676–682. https://doi.org/10.1038/nmeth.2019.

50. Brennan, C.W., Verhaak, R.G.W., McKenna, A., Campos, B., Noushmehr, H., Salama, S.R., Zheng, S., Chakravarty, D., Sanborn, J.Z., Berman, S.H., et al. (2013). The Somatic Genomic Landscape of Glioblastoma. Cell *155*, 462–477. https://doi.org/10.1016/J.CELL.2013.09.034.

51. de Bruijn, I., Kundra, R., Mastrogiacomo, B., Tran, T.N., Sikina, L., Mazor, T., Li, X., Ochoa, A., Zhao, G., Lai, B., et al. (2023). Analysis and Visualization of Longitudinal Genomic and Clinical Data from the AACR Project GENIE Biopharma Collaborative in cBioPortal. Cancer Res *83*, 3861–3867. https://doi.org/10.1158/0008-5472.CAN-23-0816.

52. Gao, J., Aksoy, B.A., Dogrusoz, U., Dresdner, G., Gross, B., Sumer, S.O., Sun, Y., Jacobsen, A., Sinha, R., Larsson, E., et al. (2013). Integrative analysis of complex cancer genomics and clinical profiles using the cBioPortal. Sci Signal *6*. https://doi.org/10.1126/SCISIGNAL.2004088/SUPPL_FILE/2004088_TABLES2.XLS.

53. Cerami, E., Gao, J., Dogrusoz, U., Gross, B.E., Sumer, S.O., Aksoy, B.A., Jacobsen, A., Byrne, C.J., Heuer, M.L., Larsson, E., et al. (2012). The cBio cancer genomics portal: an open platform for exploring multidimensional cancer genomics data. Cancer Discov *2*, 401–404. https://doi.org/10.1158/2159-8290.CD-12-0095.

54. Warnes, G.R., Bolker, B., Bonebakker, L., Gentleman, R., Huber, W., Liaw, A., Lumley, T., Maechler, M., Magnusson, A., Moeller, S., et al. (2024). Various R Programming Tools for Plotting Data [R package gplots version 3.2.0]. CRAN: Contributed Packages. https://doi.org/10.32614/CRAN.PACKAGE.GPLOTS.

55. ggplot2: Elegant Graphics for Data Analysis (3e) https://ggplot2-book.org/.

807 56. Neuwirth, E. (2022). ColorBrewer Palettes [R package RColorBrewer version 1.1-3]. CRAN:
808 Contributed Packages. https://doi.org/10.32614/CRAN.PACKAGE.RCOLORBREWER.

809 57. Kumar, A., Mitchener, J., King, Z.A., and Metallo, C.M. (2020). Escher-Trace: A web application
810 for pathway-based visualization of stable isotope tracing data. BMC Bioinformatics *21*, 1–10.
811 https://doi.org/10.1186/S12859-020-03632-0/FIGURES/4.

812 58. Subramanian, A., Tamayo, P., Mootha, V.K., Mukherjee, S., Ebert, B.L., Gillette, M.A.,
813 Paulovich, A., Pomeroy, S.L., Golub, T.R., Lander, E.S., et al. (2005). Gene set enrichment
814 analysis: a knowledge-based approach for interpreting genome-wide expression profiles. Proc
815 Natl Acad Sci U S A *102*, 15545–15550. https://doi.org/10.1073/PNAS.0506580102.

816

Figure 1

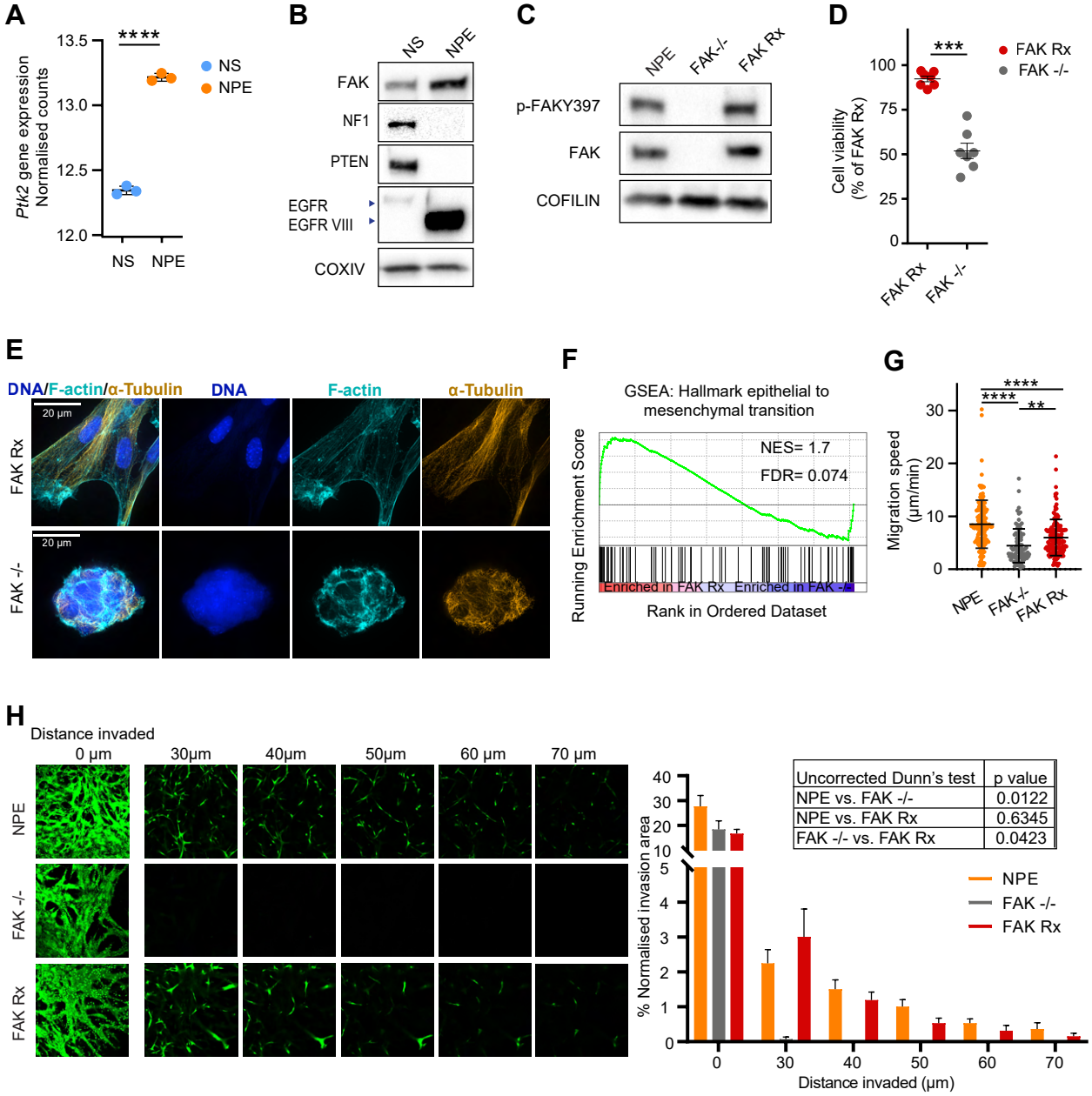

Uncorrected Dunn's test	p value
NPE vs. FAK -/-	0.0122
NPE vs. FAK Rx	0.6345
FAK -/- vs. FAK Rx	0.0423

Figure 1: Genetic deletion of FAK drives phenotypic and transcriptional changes in a mouse model of GBM stem cells.
(A) Regularised-logarithm transformation (Rlog) normalised counts of *Ptk2* in NS and NPE cells. Data obtained from (PMID: 33857425). Mean and SD are shown. Statistics: unpaired two-tailed t-test (n=3).
(B) Western blot showing FAK, NF1, PTEN, EGFR, and EGFRVIII expression in NS and NPE cells. COXIV was used as a loading control.
(C) Western blot analysis showing expression of p-FAK Y397 and FAK in NPE, FAK -/-, and FAK Rx cells. COFILIN was used as a loading control.
(D) Cell viability of FAK Rx and FAK -/- cultured for 3 days at normal culture condition. Mean and SEM are shown. Statistics: unpaired two-tailed t-test (n=7).
(E) Representative super-resolution microscopy images for FAK Rx and FAK -/- cells showing the F-actin cytoskeleton labelled with fluorophore-conjugated Phalloidin (green), α-tubulin (orange) and nuclei labelled with 40,6-diamidino-2-phenylindole (DAPI; blue). Images brightness/contrast were autoscaled individually to enable visualisation. The scale bar is 20 µm.
(F) Gene set enrichment analysis (GSEA) plot of the hallmark epithelial to mesenchymal transition gene set for proteins differentially regulated in FAK Rx cells compared to FAK -/- cells (n=3). Normalised enrichment score [NES] and false discovery rate [FDR] reported.
(G) Migration speed (µm/min) of NPE, FAK -/- and FAK Rx cells plated on laminin I and imaged every 10 min for 48 hrs. Each dot represents a cell, data from 2 independent cultures. Mean and SD are shown. Statistics: Kruskal-Wallis test followed by Dunn's multiple comparison test.
(H) Representative optical sections of NPE, FAK -/- and FAK Rx cells stained with Calcein AM invading through Matrigel. Right panel: the percentage of cells present in each displayed optical section of total cell area throughout the Matrigel (n=3 technical repeats). Mean and SD are shown. Statistics: Kruskal-Wallis test followed by Uncorrected Dunn's test.

Figure 2

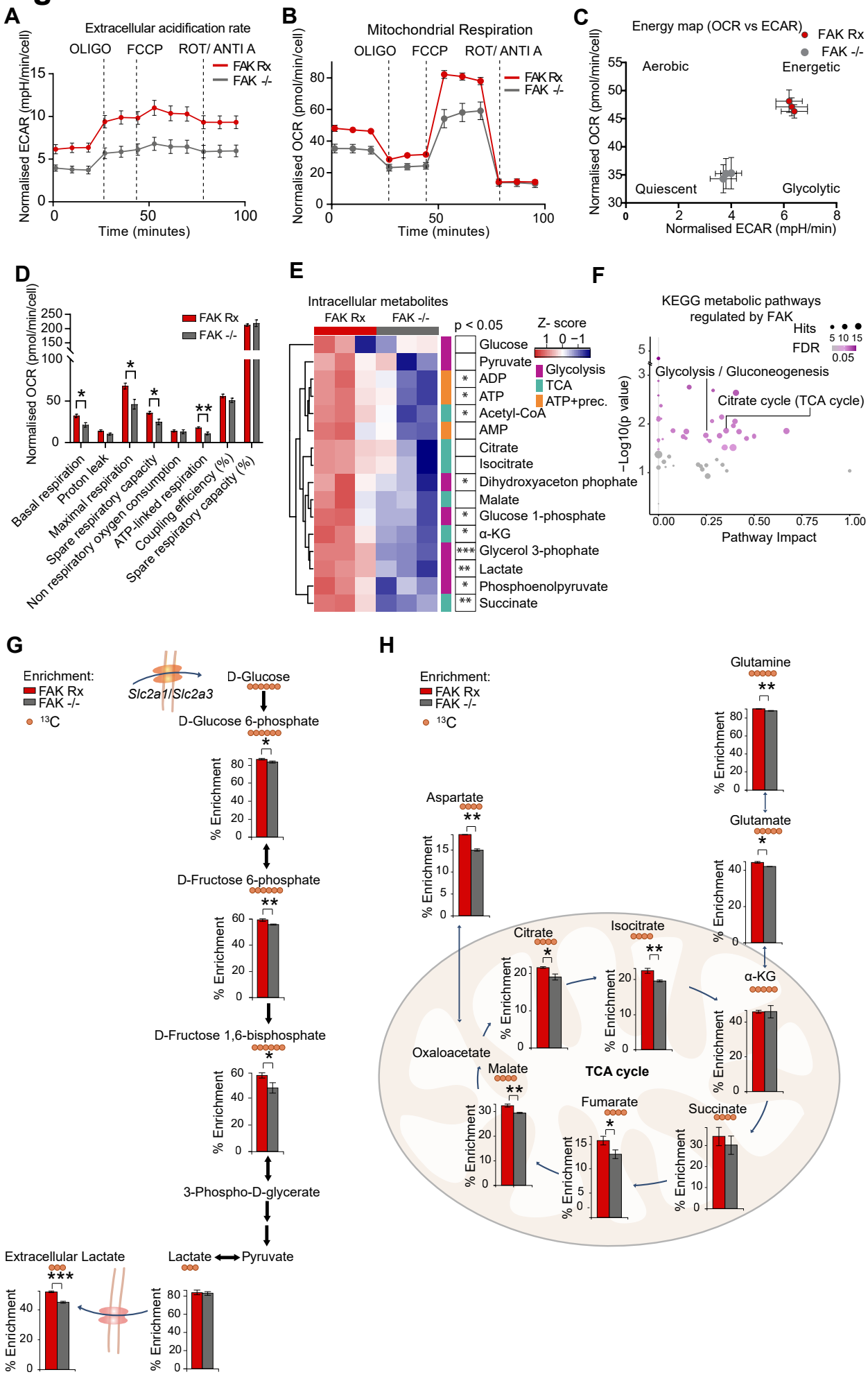
A
Extracellular acidification rate
OLIGO
FCCP
ROT/ ANTI A
FAK Rx
FAK -/-
Normalised ECAR (mpH/min/cell)
Time (minutes)
B
Mitochondrial Respiration
Normalised OCR (pmol/min/cell)
C
Energy map (OCR vs ECAR)
Aerobic
Energetic
Quiescent
Glycolytic
Normalised ECAR (mpH/min)
D
Basal respiration
Proton leak
Maximal respiration
Spare respiratory capacity
Non respiratory oxygen consumption
ATP-linked respiration
Coupling efficiency (%)
Spare respiratory capacity (%)
E
Intracellular metabolites
p < 0.05
Z- score
Glucose
Pyruvate
ADP
ATP
Acetyl-CoA
AMP
Citrate
Isocitrate
Dihydroxyaceton phophate
Malate
Glucose 1-phosphate
α-KG
Glycerol 3-phophate
Lactate
Phosphoenolpyruvate
Succinate
Glycolysis
TCA
ATP+prec.
F
KEGG metabolic pathways regulated by FAK
Hits
FDR
Glycolysis / Gluconeogenesis
Citrate cycle (TCA cycle)
−Log10(p value)
Pathway Impact
G
Enrichment:
FAK Rx
FAK -/-
13C
Slc2a1/Slc2a3
D-Glucose
D-Glucose 6-phosphate
D-Fructose 6-phosphate
D-Fructose 1,6-bisphosphate
3-Phospho-D-glycerate
Extracellular Lactate
Lactate
Pyruvate
% Enrichment
H
Glutamine
Glutamate
Aspartate
Citrate
Isocitrate
α-KG
Oxaloacetate
Malate
TCA cycle
Fumarate
Succinate

Figure 2: FAK promotes glycolysis and Mitochondria function.
Extracellular acidification rate (ECAR) (A) and oxygen consumption rate (OCR) (B) of FAK Rx and FAK -/- cells (7k cells per well, n=7 independent cultures, 3 replicate measures). Mean and SEM are shown.
(C) Basal ECAR vs OCR, calculated from data in(A) and (B). Mean and SEM are shown.
(D) Quantification of mitochondrial parameters calculated from the data in (B). Statistics: Mann-Whitney test. Mitochondrial stress test conditions: basal, oligomycin (OLIGO), Carbonyl cyanide-4 (trifluoromethoxy) phenylhydrazone (FCCP), a mixture of rotenone (ROT) and antimycin A (ANTI A). Mean and SEM are shown. Statics: Mann-Whitney test.
(E) Heatmap of glycolysis, TCA, ATP and ATP precursors normalised peak intensity in FAK Rx cells and FAK -/- cells. Each square represents an individual replicate (n = 3 independent cultures on the same day). Statistics: unpaired two-tailed t-test
(F) Bubble plot showing the glycolysis/glucogenesis and TCA cycle are among the significantly enriched KEGG pathways in pathway enrichment analysis of intracellular metabolites in FAK Rx compared to FAK -/- cells. Circles size is proportional to the number of hits in that pathway. Darker colour represents more significance.
The atom fraction enrichment of glucose-derived $^{13}C_6$ in glycolysis intermediates after incubation of FAK Rx and FAK -/- cells with $^{13}C_6$ D-glucose for 1 h (G) or $^{13}C_5$ glutamine for 3h (H) (n = 3 independent cultures on the same day). The main isotopologue of each metabolite is shown and plotted as the fraction of the sum of all isotopologues. Mean and SD are shown. Statistics: unpaired two-tailed t-test.

Figure 3

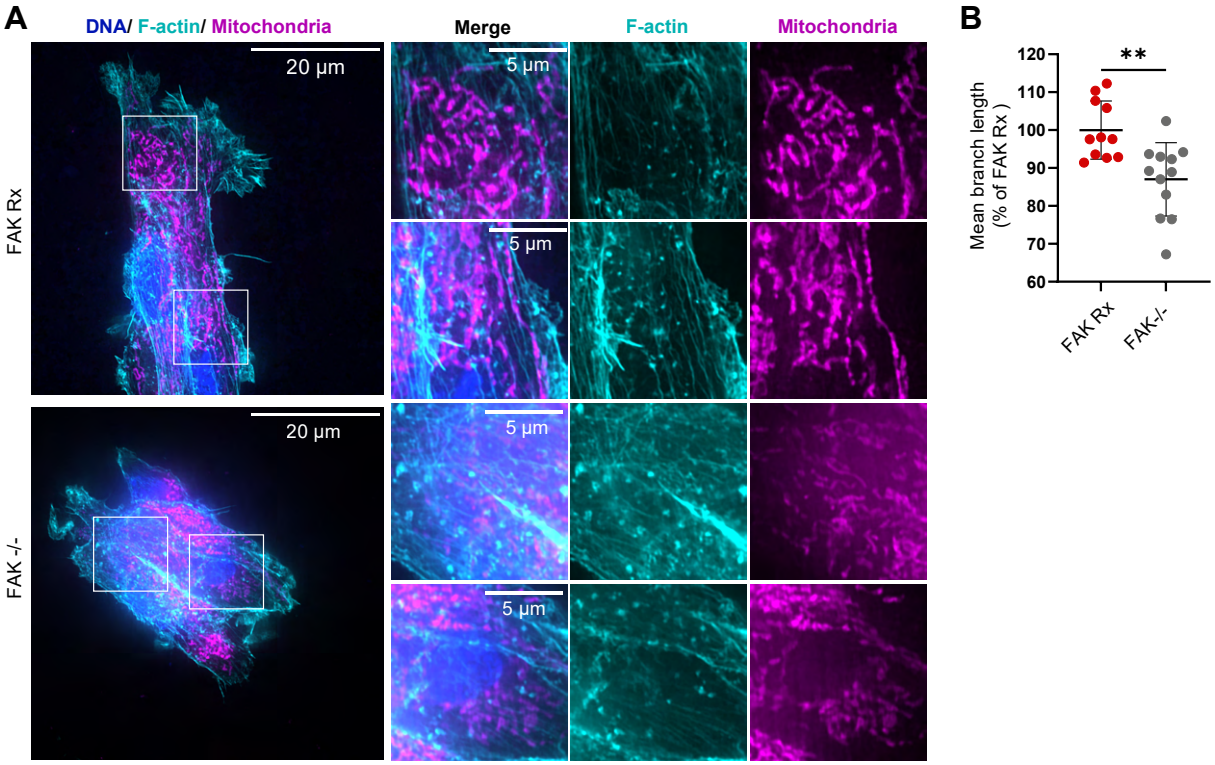

Figure 3: FAK is associated with elongated mitochondria.

(A) Representative super-resolution microscopy images for FAK Rx and FAK -/- cells showing mitochondrial morphology stained with MitoTracker Deep Red FM (magenta), the F-actin cytoskeleton labelled with fluorophore-conjugated phalloidin (cyan), and nuclei labelled with DAPI (blue). Scale bar is 20 µm in the full field of view and 5 µm in insets.
(B) Quantification of mitochondrial mean fragment length in FAK Rx and FAK -/- cells. n = 2 independent experiments. Each dot represents a field of view. Mean and SD are shown. Statistics: unpaired two-tailed t-test.

Figure 4

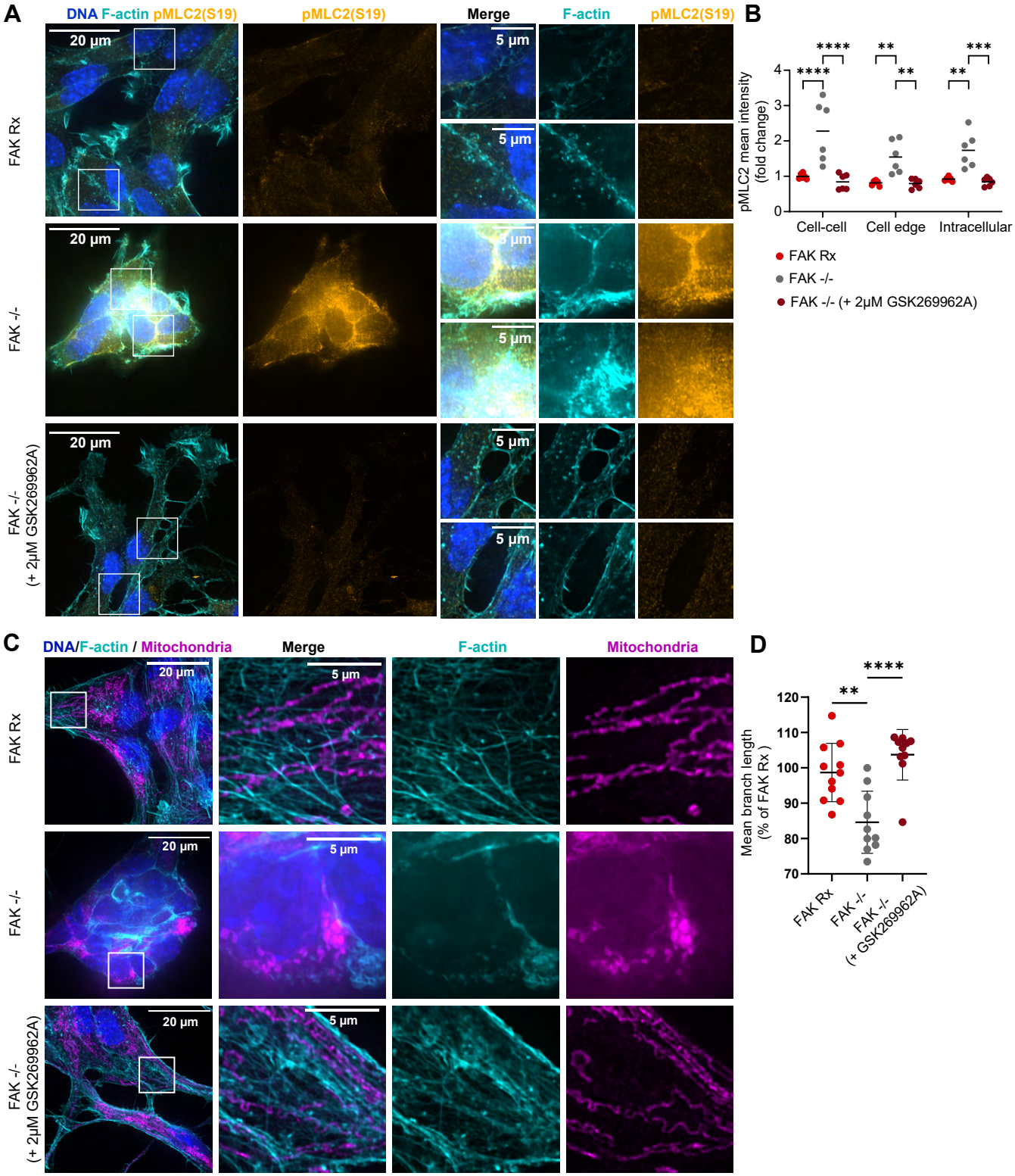

Figure 4: FAK regulates mitochondria morphology through ROCK-pMLC2 S(19) pathway.
(A) Representative super-resolution microscopy images for FAK Rx, FAK -/- cells treated with or without 2 µM GSK269962A showing pMLC2 (S19) (yellow), the actin cytoskeleton labelled with fluorophore-conjugated Phalloidin (cyan) and nuclei labelled with DAPI (blue). Cell-cell contacts are shown in insets. Scale bar is 20 µm in the full field of view and 5 µm in insets.
(B) Quantification of pMLC2 (S19) mean fluorescence intensity at cell-cell contacts, cell edge and intracellularly. n = 2 independent experiments. Each dot represents a field of view. Mean and SD are shown. Statistics: two way ANOVA followed by Tukey's multiple comparisons test.
(C) Representative super-resolution microscopy images for FAK Rx, FAK -/- cells treated with or without 2 µM GSK269962A showing mitochondrial morphology stained with MitoTracker Deep Red FM (magenta), the F-actin cytoskeleton labelled with fluorophore-conjugated phalloidin (cyan), and nuclei labelled with DAPI (blue). Scale bar is 20 µm in the full field of view and 5 µm in insets.
(D) Quantification of mitochondrial mean fragment length in FAK Rx and FAK -/- cells with or without 2 µM GSK269962A. n = 2 independent experiments. Each dot represents a field of view. Mean and SD are shown. Statistics: one way ANOVA followed by Tukey's multiple comparisons test.

Figure 5

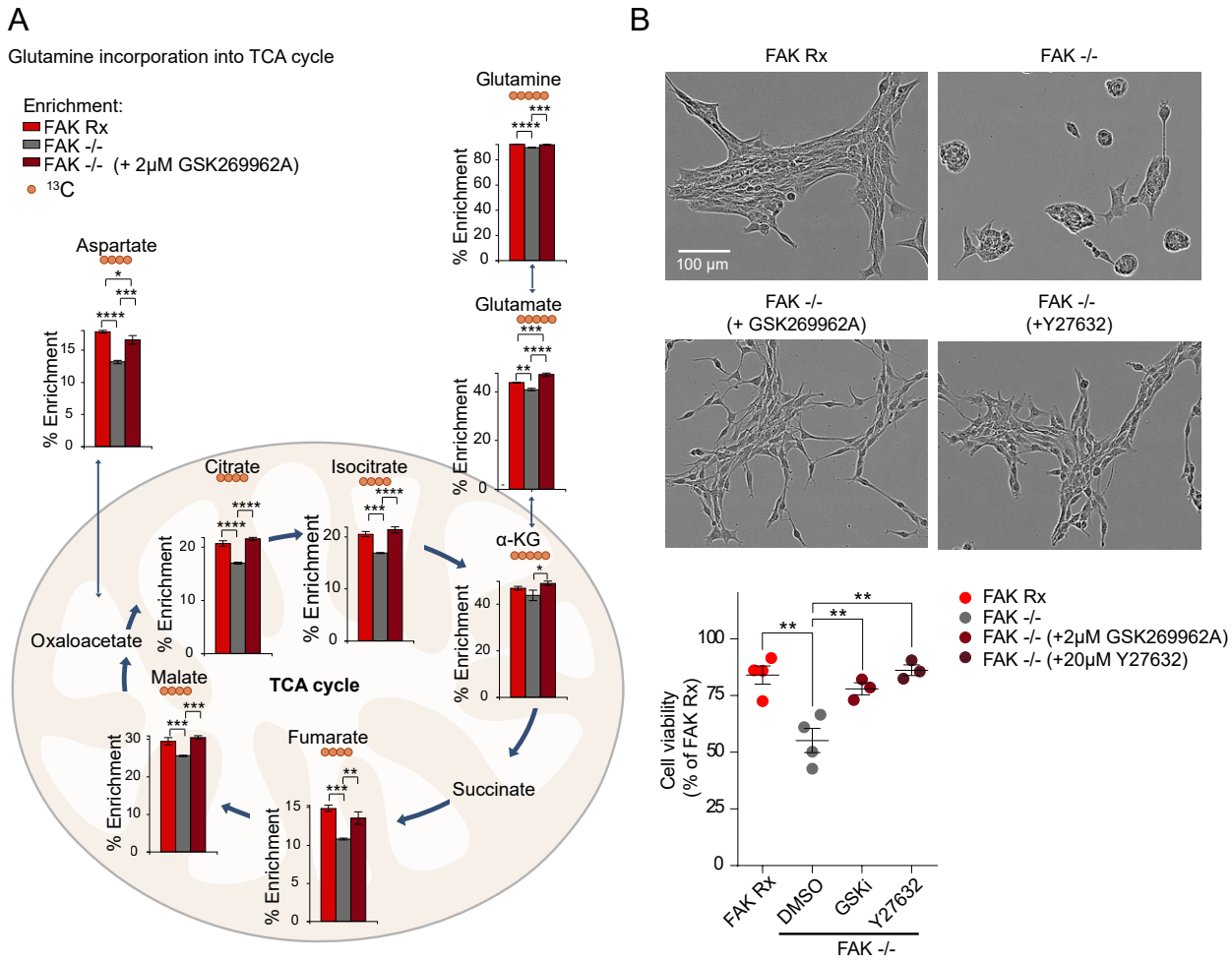

Figure 5: Treating FAK -/- cells with ROCK inhibitor GSK269962A increases glutamine incorporation into TCA cycle.
(A) The atom fraction enrichment of glutamine-derived ^{13}C in TCA intermediates in FAK Rx, FAK -/- and FAK -/- cells treated with or without 2 μM GSK269962A after 3 h incubation with $^{13}C_5$ glutamine supplemented medium. The main isotopologue of each metabolite is shown and plotted as the fraction of the sum of all isotopologues. Mean and SD are shown. Statistics: one-way ANOVA with a Tukey multiple test correction (n = 3 independent cultures on the same day).
(B) Top panel, representative phase-contrast images of FAK Rx, FAK -/- treated with and without ROCK inhibitors (+2μM GSK269962A and +20μM Y27632) for 3 days. Cell viability of FAK Rx, FAK -/- treated with and without ROCK inhibitors (+2μM GSK269962A and 20μM Y27632) for 3 days. Mean and SEM are shown. Statistics: one-way ANOVA with a Dunnett multiple test correction (n=>3 independent experiments).

Figure 6

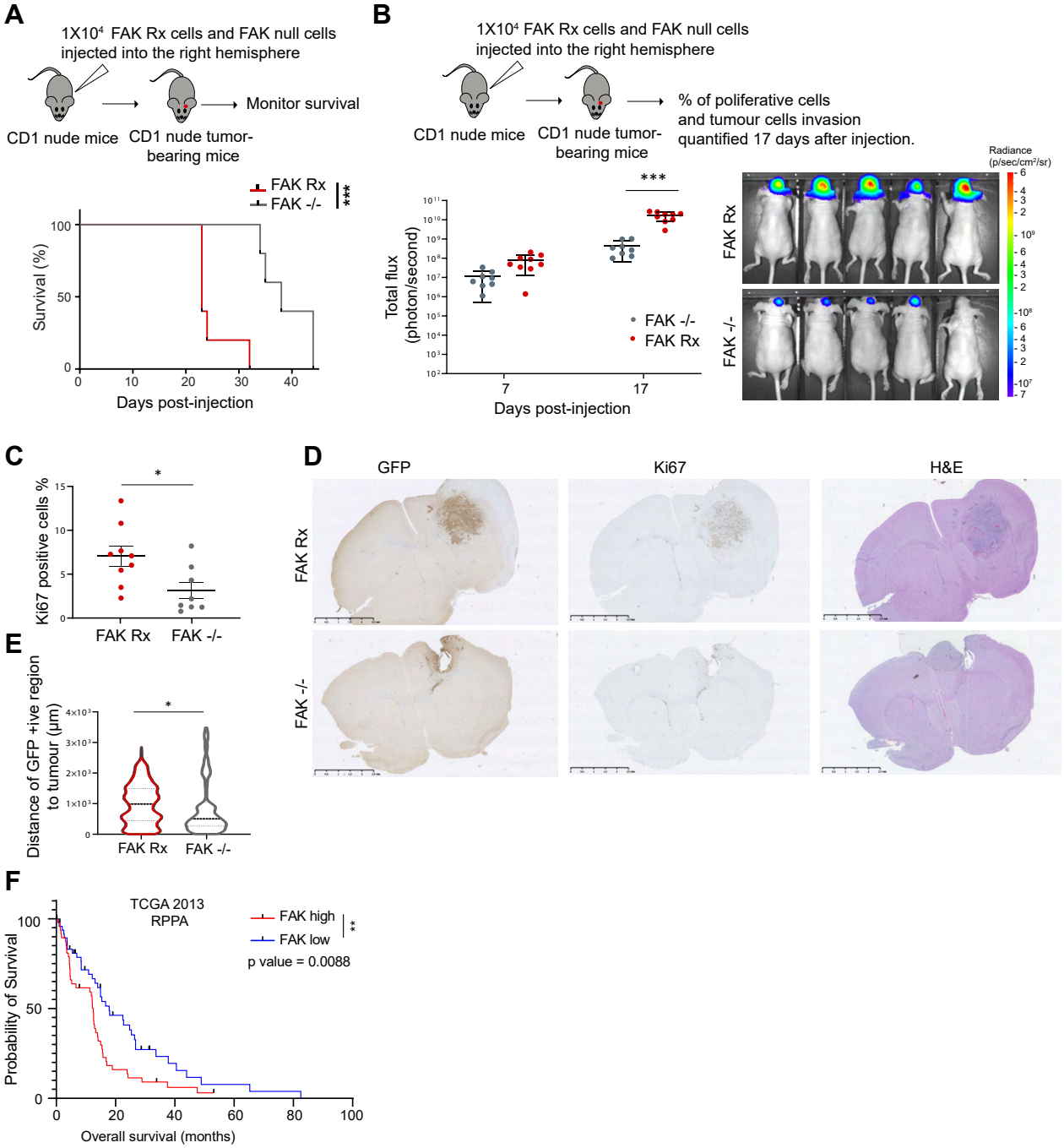

	Median survival (months)
FAK high (n=50)	12.48
FAK low (n=48)	17.84

Figure 6: FAK protein correlates with worse overall survival in vivo and in GBM patients.
(A) Kaplan-Meier curve of CD1-nude mice bearing intracranial tumours from injecting FAK Rx and FAK -/- cells. Statistics: Mantel-Cox test, n=5 for each group.
(B) Total body flux of CD1-nude mice bearing intracranial tumours from injecting luciferase- expressing FAK Rx (n=9 mice) and FAK null cells (n=8 mice) at 7 and 17 days after injection measured by IVIS imaging. Mean and SEM are shown. Statistics: 2-way ANOVA with Tukey post hoc adjustment for multiple comparisons. Right panel: representative in vivo bioluminescent images of CD1-nude mice bearing tumours from injecting FAK Rx and FAK null cells at day 17. The heat map superimposed over the mouse heads represents the radiance (photons/s/cm2/sr).
(C) Percentage of KI67 + cells in sections of intracranial tumours from injecting FAK Rx (n=9 mice) and FAK null cells (n=8 mice) at 17 days after injection. Mean and SEM are shown. Statistics: unpaired two-tailed t-test.
(D) Distance of GFP+ tumour cells to tumour edge in sections of intracranial tumours from injecting FAK Rx (n=4) and FAK null cells (n=4) at day 17 after injection. Mean and SEM are shown. Statistics: unpaired two-tailed t-test.
(E) Representative images of the immunohistochemical (IHC) staining for GFP, Ki67 and H&E stained intracranial tumours from injecting FAK Rx (n=9 mice) and FAK null cells (n=8 mice) at 17 days after injection.
(F) Kaplan-Meier curve showing the overall survival of GBM patients (n = 98) stratified into two groups representing higher (n=50) and lower quartile (n=48) FAK protein levels measured by RPPA. Data obtained from the TCGA database accessed using cBioPortal. Mean overall survival decreased by in patients with tumours expressing higher FAK protein levels. Statistics: log rank test.

Figure S1

A

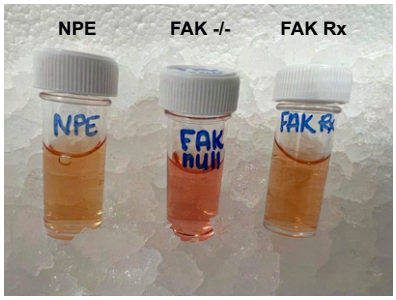

B

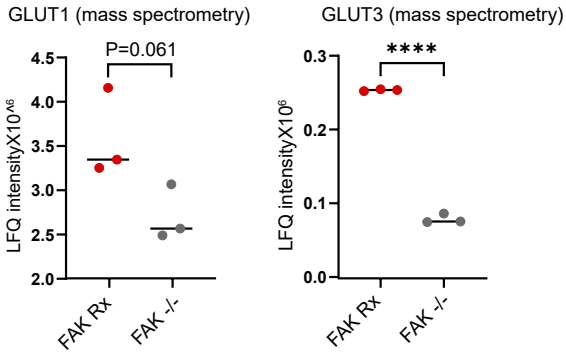

C

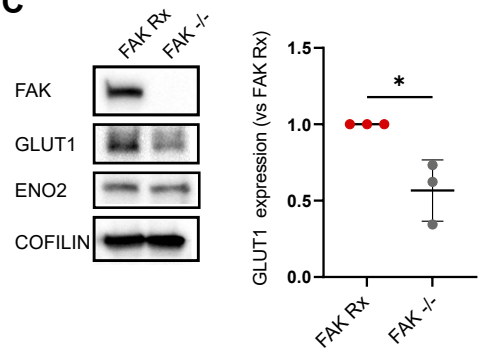

Figure S1: FAK loss is associated with less acidic culture media and reduced Glut1 and Glut3 expression.
(A) Representative images of NPE, FAK -/- and FAK Rx culture media, containing the pH indicator phenol red.
(B) Label-free quanification (LFQ) mass spectrometrey intensity of GLUT1 and GLUT3 in FAK Rx and FAK -/- cells. Statistics: unpaired two-tailed t-test.
(C) Western blot showing FAK, GLUT1, ENO2 expression. COFILIN was used as a loading control. Right panel; quantification of normalised GLUT1 expression from 3 independent experiments. Statistics: unpaired two-tailed t-test.

Figure S2

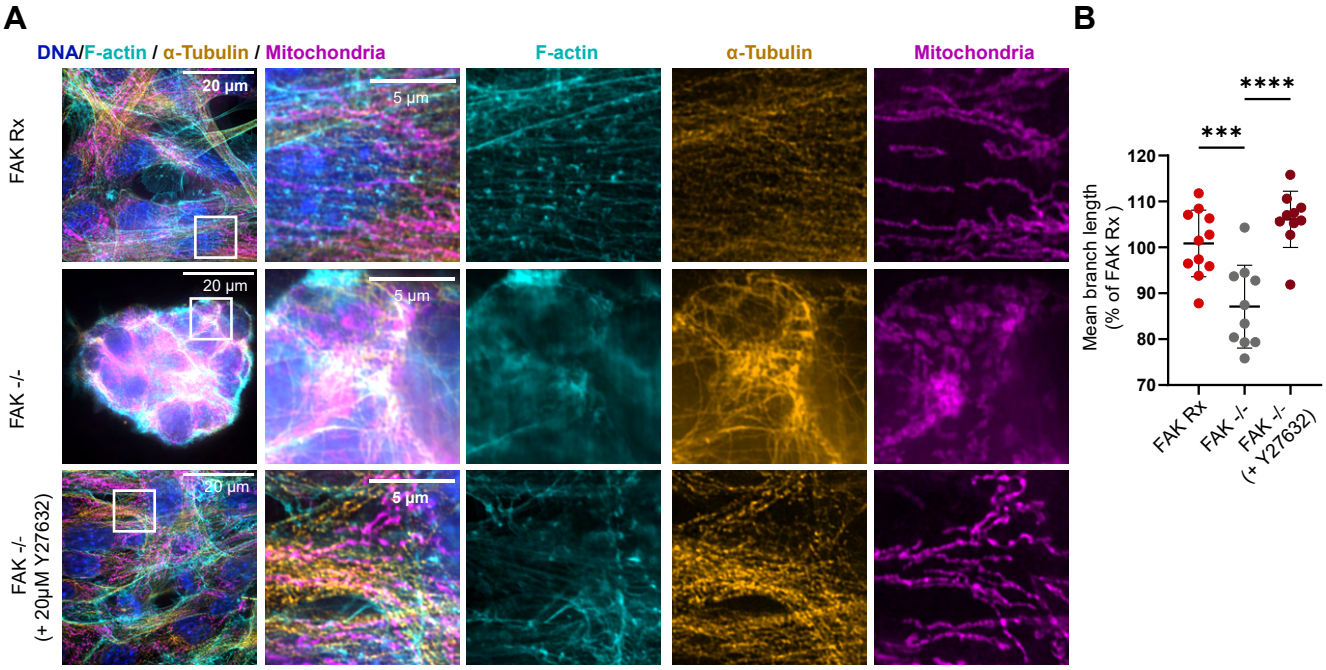

Figure S2: FAK regulates mitochondria morphology through ROCK-pMLC2 S(19) pathway.
(A) Representative super-resolution microscopy images for FAK Rx, FAK -/- cells treated with or without 20 μM Y27632 showing mitochondrial morphology stained with MitoTracker Deep Red FM (magenta), the F-actin cytoskeleton labelled with fluorophore-conjugated phalloidin (cyan), α-Tubulin (orange) and nuclei labelled with DAPI (blue). Scale bar is 20 μm in the full field of view and 5 μm in insets.
(B) Quantification of mitochondrial mean fragment length in FAK Rx and FAK -/- cells with or without 20 μM Y27632. n = 2 independent experiments. Each dot represents a field of view. Mean and SD are shown. Statistics: one way ANOVA followed by Tukey's multiple comparisons test.

Figure S3

A

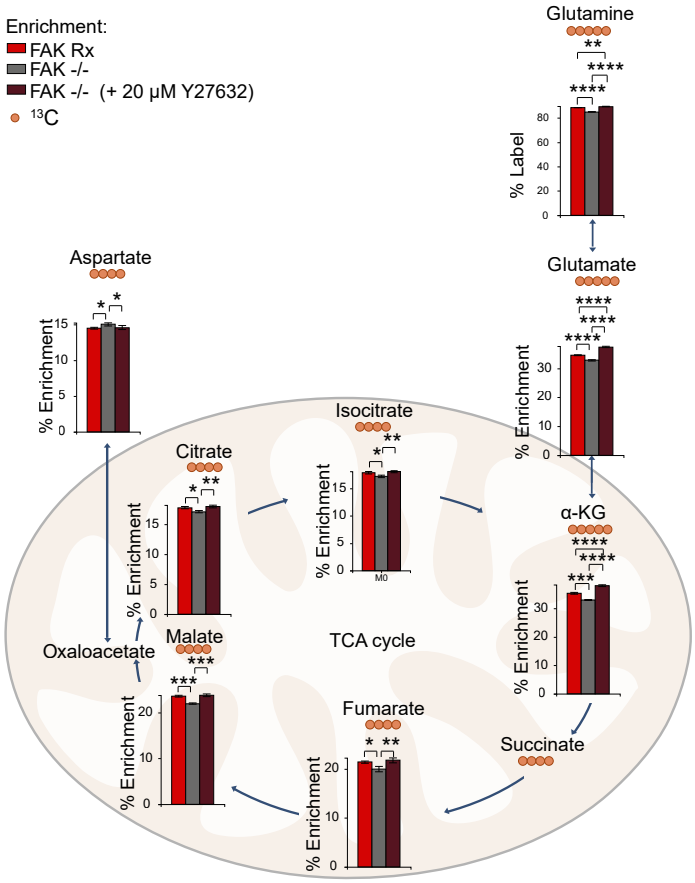

Figure S3: Treating FAK -/- cells with ROCK inhibitor Y27632 increases glutamine incorporation into TCA cycle.
(A) The atom fraction enrichment of glutamine-derived ^{13}C in TCA cycle intermediates after incubation of FAK Rx and FAK -/- cells with $^{13}C_5$ glutamine for 3h. The main isotopologue of each metabolite is shown and plotted as the fraction of the sum of all isotopologues. Mean and SD are shown. Statistics: one-way ANOVA with a Tukey multiple test correction (n = 3 independent cultures on the same day).